Geophysical Research Letters

Supporting Information for

Quantifying Sources and Sinks of Reactive Gases in the Lower Atmosphere using Airborne Flux Observations

G. M. Wolfe[1,2*], T. F. Hanisco[1], H. L. Arkinson[3], T. P. Bui[4], J. D. Crounse[5], J. Dean-Day[4,6], A. Goldstein[7], A. Guenther[8], S. R. Hall[9], G. Huey[10], D. J. Jacob[11,12], T. Karl[13], P. S. Kim[11], X. Liu[10], M. R. Marvin[3,14], T. Mikoviny[15], P. K. Misztal[7], T. B. Nguyen[5], J. Peischl[16,17], I. Pollack[16,17], T. Ryerson[16], J. M. St. Clair[5], A. Teng[5], K. R. Travis[11], K. Ullmann[9], P. O. Wennberg[5,18], and A. Wisthaler[15,19]

[1]Atmospheric Chemistry and Dynamics Laboratory, NASA Goddard Space Flight Center, Greenbelt, MD, USA

[2]Joint Center for Earth Systems Technology, University of Maryland Baltimore County, Baltimore, MD, USA

[3]Department of Oceanic and Atmospheric Science, University of Maryland, College Park, MD, USA

[4]Atmospheric Chemistry and Dynamics Branch, NASA Ames Research Center, Moffett Field, CA, USA

[5]Division of Geological and Planetary Sciences, California Institute of Technology, Pasadena, CA, USA

[6]Bay Area Environmental Research Institute, Petaluma, CA, USA

[7]Department of Environmental Science, Policy and Management, University of California at Berkeley, Berkeley, CA, USA

[8]Atmospheric Sciences and Global Change Division, Pacific Northwest National Laboratory, Richland, WA, USA

[9]Atmospheric Chemistry Division, National Center for Atmospheric Research, Boulder, CO, USA

[10]School of Earth and Atmospheric Sciences, Georgia Institute of Technology, Atlanta, GA, USA

[11]Department of Earth and Planetary Sciences, Harvard University, Cambridge, MA, USA

[12]School of Engineering and Applied Sciences, Harvard University, Cambridge, MA, USA

[13]Institute for Meteorology and Geophysics, University of Innsbruck, Innsbruck, Austria

[14]Department of Chemistry, University of Maryland, College Park, MD, USA

[15]Department of Chemistry, University of Oslo, Oslo, Norway

[16]Chemical Sciences Division, NOAA Earth System Research Laboratory, Boulder, CO, USA

[17]Cooperative Institute for Research in Environmental Sciences, University of Colorado Boulder, Boulder, CO, USA

[18]Division of Engineering and Applied Science, California Institute of Technology, Pasadena, CA, USA

[19]Institute of Ion Physics and Applied Physics, University of Innsbruck, Innsbruck, Austria

*Correspondence to: glenn.m.wolfe@nasa.gov

Contents of this file

Introduction

This document provides detailed information on the following:

S1. Sampling strategy and observations;
S2. Methods for calculation of eddy covariance and wavelet fluxes, including spectral analysis and error estimation ;
S3. Calculation of advection and storage terms for mass balance;
S4. Chemical budget calculations for isoprene, hydrogen peroxide, NOx, ozone, PAN and isoprene oxidation products;
S5. Calculation of entrainment velocities;
S6. The resistance parameterization used to derive the upper-limit H_2O_2 deposition velocity;
S7. Model descriptions for GEOS-Chem and the UWCM 0-D box model; and
S8. References.

S1. Flight and Measurements

The Studies of Emissions and Atmospheric Composition, Clouds and Climate Coupling by Regional Surveys (SEAC^{4}RS) mission was a NASA-led, multi-aircraft field campaign conducted during August and September 2013 (http://www.nasa.gov/mission_pages/seac4rs). Flights were based mostly out of Houston, Texas and focused on a wide range of environmental processes throughout the troposphere and lower stratosphere. For this study, we utilize observations collected on the NASA DC-8 during a research flight on 06 September 2013. A detailed map of the Ozarks study area is provided in Fig. S1. The flight pattern consisted of a series of four stacked, level legs within the mixed layer at mean altitudes of 311, 434, 802 and 1102 m above ground level (Fig. S3A). The DC-8 air speed was 132 – 142 m s^{-1} for each leg. The terrain in this region consists of rolling hills, with ground altitude varying between 200 – 350 m above sea level over the flux segments. The area is sparsely populated and covered in dense forest with numerous small waterways. Figure S2 shows model-estimated leaf area index (LAI) and isoprene emission factors for the area directly underneath the flight track. The mean LAI is 6.9 m^2 m^{-2}.

The DC-8 instrumental payload is substantial, and we utilize only a subset of these observations to calculate EC fluxes and derived quantities. Table S1 and references therein describe the instruments used to obtain these measurements. In all cases, we use the fastest data provided by each instrument. Signal averaging times vary from 0.5 – 20 Hz, and several instruments sample in a "disjunct" mode that results in gaps between individual observations. We assess the potential impacts of sampling strategy on flux quality in Section S2.3.

We use a number of additional measurements for chemical calculations and as input to a 0-D box model. These include photolysis frequencies measured via spectroradiometry [*Petropavlovskikh et al.*, 2007], formaldehyde measured by laser-induced fluorescence [*Cazorla et al.*, 2015], carbon monoxide measured by IR absorption (https://cloud1.arc.nasa.gov/solve/payload/dc8/dacom.html), methyl vinyl ketone and methacrolein measured by proton transfer reaction mass spectrometry [*de Gouw and Warneke*, 2007], aerosol composition from an aerosol mass spectrometer [*Jimenez et al.*, 2003], particle size distributions from an ultra-high sensitivity aerosol size spectrometer (http://www.dropletmeasurement.com/products/airborne/UHSAS-a) and a scanning mobility particle

sizer (http://science.larc.nasa.gov/large/instruments.html), and standard meteorological parameters including temperature, pressure and relative humidity. Further information on observations is available under the SEAC^{4}RS DOI at 10.5067/Aircraft/SEAC4RS/Aerosol-TraceGas-Cloud.Figure S3 shows 1 Hz time series for all key observations during the Ozarks transects. Gaps in some measurements are due to normal instrument operation (e.g. calibration and background measurements). Consistent with our discussion in the main text, the region to the east exhibits elevated ozone, NO_x, PAN and H_2O_2, while the cleaner region to the West is elevated in isoprene and its oxidation products. Lagrangian back trajectories (not shown) indicate that air in the eastern region passed over several power plants to the southeast prior to entering the Ozarks. Also notable is the reduced variability of vertical wind with increasing altitude in the mixed layer (Fig. S3C) and the fall-off in concentrations of many trace gases as the aircraft enters the free troposphere (FT) after 14:25 local time.

Vertical profiles of temperature and trace gases (Fig. S4) are typical for a well-mixed continental convective boundary layer (CBL). The temperature profile gives a lapse rate of 8 K km^{-1}, indicating moderately unstable conditions. The CBL is well-mixed for most species, and higher variability is seen in many gases at the top level due to entrainment of relatively clean air from the FT. Some species do exhibit apparent vertical variability, notably ISOPOOH + IEPOX and NO_2. Given that the CBL mixing timescale of ~11 minutes (see below) is on the order of the time between each leg, we posit that these differences represent net chemical production or destruction in the mixed layer rather than a true vertical gradient. This is a key assumption in the calculation of the storage term (Sect. S3).

Accurate flux calculations rely on the quality of vertical wind measurements, which fundamentally depend on separating 1) the motion of the wind field with respect to the aircraft and 2) the motion of the aircraft with respect to the Earth. Later in this flight, roll-pitch-yaw ("box, porpoise and crab") maneuvers were conducted at an altitude of 630 - 700 m (within the CBL) to calibrate the radome pressure system. Figure S5 shows the aircraft attitude during these maneuvers along with the derived vertical wind velocity. During the roll maneuver (first 60 seconds), correlation of aircraft and vertical velocities reflects the response of aircraft motion to strong turbulence. The data demonstrate generally minimal/negligible bleed-through of aircraft motions even for large aircraft vertical velocities. During flux segments, the aircraft vertical velocity was within the range of ±4 m s^{-1}, the yaw angle varied by less than 3° and the roll angle by less than 10°.

S2. Flux Calculations

Both traditional eddy covariance and wavelet transforms were performed for each of the four segments indicated in Fig. S3. Fluxes reflect processes occurring upwind of the measurement as the turbulent field is advected with the horizontal wind. The scale of the flux footprint can be gauged via its half-width, $dx_{0.5}$, which is defined as the horizontal length beyond which less than 50% of the surface flux is measured [*Karl et al.*, 2013; *Weil et al.*, 1992].

$$dx_{0.5} = 0.9\frac{\overline{U} z_m^{2/3} h^{1/3}}{w^*} \qquad (1)$$

Here, $\overline{U}$ is the horizontal wind speed, z_m is the measurement height and h is the boundary layer height. The convective velocity scale, w*, is defined as [*Arya*, 1988]:

$$w^* = \left(\frac{gh}{\theta_0}\langle w'\theta'\rangle_0\right)^{1/2} \qquad (2)$$

where g is the gravitational constant, θ_0 is surface potential temperature, and $\langle w'\theta' \rangle_0$ is the surface kinematic heat flux (determined by extrapolation of the observed heat flux profile). For this flight, we calculate w* = 1.7 m s^{-1} and footprint half-widths of 0.6, 1.0, 1.4 and 2.1 km. Given the homogeneity of the region upwind of the transect, we do not expect the increase of footprint size with height to introduce significant errors in flux divergence calculations. Division of the CBL height by w* gives a characteristic mixing (CBL turnover) timescale of 11 min.

S2.1 Eddy Covariance

Eddy covariance (EC) is a well-established technique for calculation of vertical fluxes of energy and trace gases in the turbulent boundary layer. The flux is defined as the time-averaged product of instantaneous deviations in vertical wind speed (*w*) and scalar magnitude (*c*).

$$Flux = \frac{1}{n}\sum_{i=1}^{n}\left(w_i - \overline{w}\right)\left(c_i - \overline{c}\right) = \langle w'c' \rangle \qquad (3)$$

Here, n is the total number of data points in the flight segment and $\overline{w}$, $\overline{c}$, w′ and c′ are the mean and fluctuating components of the instantaneous measured values w_i and c_i. More details on EC analysis and applications can be found elsewhere [*X Lee et al.*, 2004]. The data analysis procedure is as follows:

1. *Averaging*: 3-D winds were averaged or sub-sampled from 20 Hz to the native time resolution of each instrument (Table S1).
2. *Rotation*: A 1-coordinate rotation was applied to force the mean vertical wind to 0 for each segment. Rotation angles were less than 5 degrees for all legs.
3. *Despiking*: Scalar data were despiked using a mean absolute deviation filter following *Mauder et al.* [2013].
4. *Detrending*: Scalar data were detrended by subtracting a 20-second running mean, corresponding to a spatial scale of ~26 km. This procedure was chosen as a compromise between removing non-turbulent variability (e.g. due to changing chemical conditions) and capturing the largest flux-contributing eddies, based on inspection of flux divergence and cospectra at a range of trend averaging windows (not shown).
5. *Time Lagging*: processed scalar data were lagged in time relative to vertical wind velocity to optimize the covariance. Figures S6A – S14A show the lagged covariance plots for all of the scalars discussed here. Lag times were generally small (< 1 second) as most instruments sampled quickly and used high-quality clock sources. For the Caltech instrument, fluxes of some species were weak and thus did not produce strong lag peaks (e.g. Fig. S14A). In this case, we apply the lags derived from H_2O_2 to all species for consistency, assuming the lag is primarily due to the offset between the recorded times of vertical wind and scalar measurements.

S2.2 Spectral Analysis

Fourier transforms provide valuable information on the contributions of different turbulent frequencies to the total flux, as well as a means to gauge potential artifacts due to instrument response or sampling strategy. Note that the maximum resolvable frequency for a Fourier transform (the Nyquist frequency) is equal to half of the native sample rate. The Fourier frequency scale can be converted to a length scale by dividing the aircraft speed, typically 132 m s^{-1}, by frequency.

Figures S6B-S14B show cospectra of scalar and vertical wind fluctuations for each flight segment. Some species exhibit intermittent "dropouts" in cospectal density (e.g. H_2O_2 (Fig. 8B) and PAN (Fig. 11B)), but these features do not appear consistently for multiple segments or for multiple species measured by the same instrument, suggesting they are not due to instrumental issues. Most cospectra illustrate an $f^{-7/3}$ slope in the inertial sub-range, consistent with theoretical expectations [*Kaimal et al.*, 1972].

Convolving the cospectra with frequency aids identification of the peak contributions to the total cospectral power (Figs. S6C-S14C). In general, we expect the cospectral peak to shift to lower frequencies with increasing altitude in the mixed layer, reflecting the shift to larger eddies. This behavior is most evident in scalars with strong surface fluxes, such as isoprene (Fig. S7C), for which the cospectral peaks in the first through third legs correspond to rough spatial scales of 1.0, 1.4 and 4.5 km. In some cases (e.g. Fig. S6C for sensible heat), a secondary peak appears at frequencies below 0.01 Hz (13 km) and likely indicates an advective contribution to the flux from mesoscale motions [*Mauder et al.*, 2007; *Sievers et al.*, 2015].

It has been suggested that reactive gases can exhibit more complex features in their cospectra due to varying timescales for their sources and sinks [*DiGangi et al.*, 2011; *Farmer and Cohen*, 2008; *Wolfe et al.*, 2009], and such features are observed in the present study. For example, isoprene oxidation products (Figs. S12C-S14C) tend to exhibit a sign change at midrange frequencies, with generally negative contributions at higher frequencies and generally positive contributions at lower frequencies. This behavior is consistent with the observed flux divergence for these compounds, which indicates deposition at the surface and production aloft. A more detailed analysis of cospectral features might permit disentanglement of these processes, providing an alternative means of quantifying surface and in situ (chemical) flux contributions.

Cumulative integrals under the cospectra, commonly referred to as ogives (Fig. S6D-S14D), provide a straightforward means of assessing systematic errors due to inadequate sampling at the high and low-frequency ends. If all relevant frequencies are adequately measured, the curves will taper to asymptotes, as in the case of sensible heat fluxes (Fig. S6D). Species that do not taper at the low frequency end (e.g. ozone, Fig. S9D) may have significant advective flux contributions. This behavior could also indicate incomplete sampling of large-scale eddies due to the length of a flight segment; however, most species do indeed show tapering at the low-frequency end, and we also assess this error explicitly below. In contrast, many species exhibit a lack of tapering at the high-frequency end, which is primarily due to the limitations imposed by the native instrument sampling rates. Such spectral artifacts can be corrected empirically using the high-frequency sensible heat cospectra as described in Sect. S2.3.

S2.3 Uncertainty Analysis

Errors in airborne fluxes arise from two main sources: sampling strategy and instrument performance. Sampling strategy refers to how well a flight segment captures a statistically robust sample of the turbulent field. Instrument-related errors include random uncertainties due to instrument sensitivity and systematic error due to limited measurement frequency and absolute calibration accuracy.

As discussed in Lenschow et al. [*Lenschow et al.*, 1994], systematic and random sampling errors in airborne EC fluxes depend primarily on the segment length and aircraft altitude.

$$systematic\ error \leq \frac{2.2h\left(z/z_i\right)^{1/2}}{L} \tag{4}$$

$$random\ error \leq 1.75\left(z/z_i\right)^{1/4}\left(z_i/L\right)^{1/2} \tag{5}$$

Here, z_i is the CBL height (1060 m), z is measurement height, h is the boundary-layer height and L is the length of the flight segment. Note that both errors are proportional to altitude and inversely proportional to leg length. For the four flux segments discussed here, we calculate systematic errors of 1.7%, 2.0%, 2.7% and 3.5% and random errors of 15%, 16%, 19% and 22%.

Precision determines the ability of an instrument to discriminate signal changes due to turbulent concentration fluctuations against background noise, which effectively defines a "flux detection limit". Analytical equations have been developed to quantify this uncertainty [*Karl et al.*, 2013; *Lenschow and Kristensen*, 1986], but these equations require specific knowledge of instrument sensitivity and integral timescales for each species. We instead develop an empirical approach to determine the flux detection limit for each flux observation. The method involves several steps, illustrated in Fig. S15:

1. Generate a white noise (random and normally-distributed) time series with the same mean, standard deviation and number of samples as the despiked/detrended scalar (c′) time series (Fig. S15B).
2. Calculate the lagged covariance of this noise vector with w′ with a sufficient number of lag points to obtain a statistical distribution of the resulting "noise covariance". Here we use a lag of ± 100 seconds (Fig. S15C).
3. Calculate the standard deviation of the lagged-covariance time series. Define this as the 1σ flux detection limit (Fig. S15D).
4. Repeat this procedure as many times as needed to obtain a stable average value for the flux detection limit. This is necessary because of the use of a random time series. Here we use 10 repetitions.

This method is akin to averaging the covariance of c′ and w′ at lags far away from that of peak covariance [*Spirig et al.*, 2005; *Wienhold et al.*, 1994] but does not require the arbitrary choice of a lag window for averaging. It inherently assumes the limiting case that all variance in c′ is due to uncorrelated noise and thus provides an upper limit for the flux detection limit. We double this value to obtain the 2σ detection limit, corresponding to a confidence interval of 95%. As an alternative estimate of inherent flux variability, we calculate the standard error of the covariance time series:

$$\overline{\sigma_F} = \frac{\text{standard deviation of } \overline{w'c'}}{\sqrt{\#\text{ of data points}}} \qquad (6)$$

Figure S16 compares the fractional 2σ uncertainty derived from these two methods for all EC flux segments. The two methods give nearly identical results in most cases.

Instrument data rates can affect the measurement of fluctuations at high frequencies, leading to a systematic underestimate of the true flux. The instruments used in this study possess a wide range of sampling frequencies (Table S1), including several "disjunct" measurements where individual data points are separated by gaps. We evaluate the measurement frequency error empirically using the high-frequency (20 Hz) potential temperature data. Fluxes for each segment are calculated using temperature data averaged to sampling intervals that mimic those of other instruments, and results are then compared to those derived from the native data rate. As shown in Figure S17 and Table S3, the difference between 20 Hz and 10 Hz is negligible, while averaging to 1 Hz reduces the flux magnitude by ~15%. This is consistent with the cospectra and ogives (Fig. S17B-C). Underestimates due to disjunct sampling are somewhat more variable but are within 15% for the lowest three legs. Disjunct cospectra also differ from "continuous" cospectra at the low frequency end, reflecting under-sampling of the largest wavelengths. Most of our analysis relies on linear fitting of the flux profiles, thus in Table S3 we also show the effect of changing data rate on the slope and intercept of the

temperature flux profile. Results are similar to those observed for individual flux values, with the most severe effects being an 11% decrease in slope and 9% decrease in intercept. While we acknowledge that this is an additional potential error source in flux measurements, we do not apply corrections for sampling rates because 1) using the results of the above analysis to do so would require spectral similarity of sensible heat and gas fluxes, which may not be valid for some reactive species, and 2) these errors are on the order of, or smaller than, random uncertainties due to sampling and precision.

All fluxes are corrected upward in magnitude for the systematic sampling error (Eq. 4). The random uncertainty for each flux measurement is taken as the root-mean-square sum of the 2σ flux detection limit and the random sampling error; these values define the error bars in Figures 3 and 4 of the main text. The calibration accuracy for all species is listed in Table S1 but is not included in the error bars. This uncertainty is inherently systematic (but of unknown sign) and would equate to a scaling factor for fluxes.

S2.4 Wavelets

Wavelet analysis is a useful tool for airborne fluxes, as it allows calculation of fluxes along a flight transect and affords a check on eddy covariance calculations. *Torrence and Compo* [1998] provide a thorough review of wavelet analysis, and *Misztal et al.* [2014] detail the application of wavelets to airborne fluxes. As in the latter study, we utilize the Morlet wavelet. Figure S18 illustrates a typical wavelet analysis. Transforms are performed on the despiked, detrended, time-lagged scalar and vertical wind time series, and the cospectral power is calculated from the cross-product of the wavelet power spectra. The result is essentially a cospectrum for each point in the measurement (Fig. S18B). As with cospectra derived from fast fourier transforms, the wavelet cospectra contain areas of positive and negative flux contributions. In the provided example, the strongest contributions to the isoprene flux appear in the central portion of the flight segment at spatial scales of several km. Integration of the cospectral power across all frequencies yields the wavelet flux along the transect (Fig. S18C). The mean wavelet flux typically agrees with the EC flux to within 10% for most species. Additionally, wavelet cospectral power can be averaged along the length/time coordinate to produce a mean wavelet cospectrum. As seen in Fig. S19, this agrees well with the cospectrum determined from Fourier transforms. Though wavelet analysis was performed for all species and flight segments, in this study we limit the discussion of these results to surface fluxes of isoprene, ozone, NO_x and H_2O_2 derived from wavelet transforms along the first transect and corrected for flux divergence between the top of the canopy (assumed to be 20 m) and the measurement height. To remove some of the variability associated with sampling individual strong eddies and better represent average surface conditions, wavelet fluxes are also smoothed with a 10 km running mean. Figure S20 maps these fluxes over a satellite image of the study area.

S3. Mass Balance Budget Calculations

As shown in Eqn. (2) of the main text, the flux divergence includes contributions from in situ production and loss (Q), horizontal mean advection (A) and storage ($\partial C/\partial t$). To use fluxes to evaluate chemistry, we must first correct for the latter two terms. Results of these calculations are shown in Table S2.

Storage, which represent the time-rate-of-change of a scalar, is estimated via least-squares fits to plots of mean mixing ratios vs mid-point time for the first three legs. As mentioned in Sect. 1, this assumes that any apparent vertical concentration gradients are actually due to changes in concentration in the CBL as a whole, which is well mixed.

Advection is typically parameterized as the product of the mean horizontal wind speed ($\overline{U}$) and the concentration gradient along this path. We decompose this into two components, one along the flight track (x) and the other perpendicular to the flight track (y).

$$A = \cos\phi\overline{U}\frac{\partial C}{\partial x} + \sin\phi\overline{U}\frac{\partial C}{\partial y} \quad (7)$$

Here, ϕ is the difference between the aircraft heading and the horizontal wind direction. For the flight segment discussed here, the wind vector was 2.6 m s^{-1} from 165°, and aircraft headings were 107° and 287°. Average along-track advection rates were calculated by fitting the observations for each of the first three legs to get the horizontal concentration gradient, multiplying by the along-track wind vector, and averaging over the three legs. Calculated advection rates are shown in Table S2. With the exception of ozone, advections rates are small compared to the flux divergence. Our sampling strategy does not provide the data necessary to estimate the cross-track advection component; however, given that the area to the south is mostly homogeneous (i.e. heavily forested), we expect this component to be even smaller than the along-track component for most species.

The chemical term, Q, is calculated as the residual of flux divergence plus storage plus advection and is also shown in Table S2. The error in Q is calculated by summing the independent errors for flux divergence, storage and advection in quadrature.

Fluxes due to storage and advection are calculated by assuming these terms are constant and integrating from the ground to the top of the CBL.

S4. Chemical Calculations

Here we summarize the chemical kinetics of the gas-phase production and loss processes considered in the derivation of the parameters described in the main text. Table S4 lists all relevant reaction rates. Rate constants are taken from the latest IUPAC recommendations [*Atkinson et al.*, 2004; 2006] and recent literature. Observed species concentrations and photolysis frequencies used in these calculations are averaged over all four flight segments unless otherwise specified. As stated above and evident in Eqn. (2) of the main text, the chemical tendency (Q) is calculated as the residual sum of flux divergence, advection and storage.

S4.1 Isoprene

Isoprene, $CH_2C(CH_3)CHCH_2$, a conjugated diene, is readily oxidized via hydroxyl radical (OH), ozone (O_3) and nitrate radical (NO_3). Addition of OH is immediately followed by reversible addition of O_2, leading to 8 potential isoprene hydroxyperoxy radical ($ISOPO_2$) isomers. Addition of ozone is somewhat more complex and can lead to multiple products, including Criegee biradicals and closed-shell carbonyls. Attack via NO_3 also proceeds through addition to a double bond; however, NO_3 is highly photolabile and thus a minor oxidant under sunny conditions and is neglected in this analysis.

$ISOP + OH\ (+O_2) \rightarrow ISOPO_2$ (R1)

$ISOP + O_3 \rightarrow$ products (R2)

The chemical loss rate for isoprene is then

$$Q(ISOP) = -k_1[OH][ISOP] - k_2[O_3][ISOP] \quad (8)$$

Rearrangement yields an equation for [OH] that depends only on observationally-derived parameters.

$$[OH] = \frac{Q(ISOP) + k_2[O_3][ISOP]}{-k_1[ISOP]} \quad (9)$$

The calculated ozone term is 11% of the total isoprene loss rate.

S4.2 Hydrogen Peroxide

Hydrogen peroxide (H_2O_2) is produced via self-reaction of hydroperoxy radicals (HO_2) and lost via reaction with OH and photolysis.

$HO_2 + HO_2 \rightarrow H_2O_2 + O_2$ (R3)

$H_2O_2 + OH \rightarrow H_2O + HO_2$ (R4)

$H_2O_2 + h\nu \rightarrow 2OH$ (R5)

The rate expression is then

$$Q(H_2O_2) = k_3[HO_2][HO_2] - k_4[OH][H_2O_2] - j_5[H_2O_2] \quad (10)$$

And rearrangement yields

$$[HO_2] = \left(\frac{1}{k_3}(Q(H_2O_2) + k_4[OH][H_2O_2] + j_5[H_2O_2])\right)^{1/2} \quad (11)$$

This equation is evaluated using OH concentrations calculated from Eqn. (9). The OH and photolysis losses are calculated to be 4% and 13%, respectively, of the net H_2O_2 chemical rate.

S4.3 Ozone

Overwhelming contributions of storage and advection to the ozone budget (Table S2) limit our ability to derive chemical parameters from the ozone flux divergence for the conditions of our study. Nonetheless, it is worthwhile to demonstrate here the potential utility of a constraint on net ozone chemistry. In the troposphere, ozone is produced via photolysis of nitrogen dioxide (NO_2) to make $O(^3P)$, which reacts rapidly with O_2. Reaction of ozone with nitric oxide (NO) regenerates NO_2. Peroxy radicals, including HO_2 and organic peroxy radicals (RO_2), can also react with NO to make NO_2.

$NO_2 + h\nu\ (+O_2) \rightarrow NO + O_3$ (R6)

$NO + O_3 \rightarrow NO_2 + O_2$ (R7)

$NO + HO_2 \rightarrow NO_2 + OH$ (R8)

$NO + RO_2 \rightarrow NO_2 + RO$ (R9)

Reactions (R6) and (R7) constitute a null cycle wherein ozone is neither produced nor lost; thus, net ozone production is effectively determined by the production of NO_2 via (R8) and (R9).

$$Q(O_3) = k_8[HO_2][NO] - k_9[RO_2][NO] \quad (12)$$

Thus, with observed [NO] and measured or calculated [HO_2] (e.g. from Eqn. (10)), one could derive the concentration of RO_2. This estimate will depend on the assumed value for k_9, which represents the average rate coefficient for the entire RO_2 pool. In this environment, the most abundant organic peroxy radicals are likely $ISOPO_2$ and CH_3O_2 [*Wolfe et al.*, 2014], for which the rate constants for reaction with NO at 298 K are 9.0 x 10^{-12} and 7.7 x 10^{-12} cm^3 s^{-1}, respectively.

S4.4 NO_x

NO_x enters the atmosphere via direct emission and is removed via conversion to higher oxides of nitrogen, including nitric acid (HNO_3), alkyl nitrates (AN) and acylperoxy nitrates (APN). Peroxyacetyl nitrate (PAN), formed from reaction of NO_2 with the peroxyacetyl radical (PA), is typically the dominant member of the APN family [*Wooldridge et al.*, 2010]. We ignore minor APNs for this calculation.

$NO_2 + OH \rightarrow HNO_3$ (R10)

$RO_2 + NO \rightarrow AN$ (R11)

$PA + NO_2 \rightarrow PAN$ (R12a)

$PAN \rightarrow PA + NO_2$ (R12b)

The nitric acid formation rate is calculated as 0.002 ± 0.001 pptv s^{-1}. AN formation is a minor channel in the reaction of RO_2 with NO, with a yield that can vary from 0 to 12% depending on RO_2 structure [*Perring et al.*, 2009]. Calculating the total AN formation rate explicitly is nontrivial due to the variety of possible RO_2 species and their associated NO reaction rates and AN yields. As an approximation, we divide the explicitly-calculated production rate of first-generation isoprene nitrates of 0.032 pptv s^{-1} (Sect. S4.6.1 and Table S5) by the fraction of ISOPN production relative to total AN production (0.81) from the 0-D box model (see Sect. S7.2) to obtain an estimated total AN production rate of 0.040 ± 0.009 pptv s^{-1}. The uncertainty in this rate is propagated from the OH concentration used to compute ISOPN production. PAN decomposition is highly temperature-sensitive, thus this compound can be a source or sink for NO_x. Analysis of PAN fluxes (see below) indicates that PAN is a net source of NO_x averaged over the boundary layer, with a rate of 0.006 ± 0.003 pptv s^{-1}. Thus we arrive at a total gas-phase NO_x loss rate of 0.035 ± 0.010 pptv s^{-1}. The NO_x loss rate from flux analysis (Table S2) is 0.024 ± 0.006 pptv s^{-1}, and the difference is then 0.011 ± 0.012 pptv s^{-1}. The AN recycling efficiency discussed in the main text is the ratio of this difference to the AN production rate and represents a theoretical fraction of NO_x released through subsequent processing of AN.

S4.5 PAN

Though not presented in the main text, fluxes of peroxyacetyl nitrate (PAN) exhibit unique vertical structure due to their strong temperature dependence [*Wolfe et al.*, 2009] and provide a useful demonstration of chemical flux calculations. Moreover, knowledge of PAN tendencies is necessary for

the above analysis of NO_x flux divergence. Here we demonstrate a method to calculate primary production of peroxyacetyl radicals (PA) using observed PAN flux divergence.

PAN ($CH_3C(O)OONO_2$) is formed via the reaction of PA with NO_2 (R12a). In the lower troposphere, thermal dissociation (R12b) is the only sink for PAN, and the decomposition rate is highly temperature-dependent. Because PAN exists in equilibrium, its net lifetime is affected by the loss of the PA radical, which can also react with NO, HO_2 and RO_2.

PA + NO → products (R13)

PA + HO_2 → products (R14)

PA + RO_2 → products (R15)

The rate laws for PAN and PA are then:

$$Q(PAN) = k_{12a}[PA][NO_2] - k_{12b}[PAN] \tag{12}$$

$$Q(PA) = P_{PA} + k_{12b}[PAN] - (k_{12a}[NO_2] + k_{13}[NO] + k_{14}[HO_2] + k_{15}[RO_2])[PA] \tag{13}$$

P_{PA} represents primary PA production from oxidation of oVOC (e.g. acetaldehyde, methacrolein, etc.). The PA lifetime is short (~30 s) compared to changes in its sources, thus we can derive a steady state PA concentration assuming Q(PA) ≈ 0:

$$[PA] = \frac{P_{PA} + k_{12b}[PAN]}{k_{12a}[NO_2] + k_{13}[NO] + k_{14}[HO_2] + k_{15}[RO_2]} \tag{14}$$

As noted by *LaFranchi et al.* [2009], under warm conditions the PAN equilibrium establishes quickly and we can simplify these equations by considering the total chemical rate for the family PAN* = PAN + PA. Also, typically PAN>>PA, so PAN* ≈ PAN. Combining Eqns. (12) – (14) and rearranging gives:

$$Q(PAN) = P_{PA} f_{PAN} - k_{12b}[PAN](1 - f_{PAN}) \tag{15}$$

$$f_{PAN} = \frac{k_{12a}[NO_2]}{k_{12a}[NO_2] + k_{13}[NO] + k_{14}[HO_2] + k_{15}[RO_2]} \tag{16}$$

Thus, PAN production (first term of Eqn. (15)) is determined by the fraction of primary PA that reacts with NO_2 (f_{PAN}) and PAN loss (second term) is determined by the fraction of PA from PAN decomposition that reacts with other radicals.

The theoretical PAN flux due to chemistry is the ground-up cumulative integral of Eqn. (15). For this calculation, we use the observed temperature profile (linearly extrapolated to the surface) but hold concentrations of PAN, NO and NO_2 constant at their CBL average values (Table S2). HO_2 and RO_2 are held fixed at 26 and 41 pptv, respectively. Under these conditions, f_{PAN} is ~0.42 throughout the boundary layer, thus we can pull this term out of the integrand. Substituting the other terms in the mass balance equation for Q(PAN) (Eqn. (1) in the main text), we derive an expression relating primary PA production to observationally-constrained quantities:

$$P_{PA} = \frac{1}{f_{PAN}} \frac{\partial}{\partial z}\left(F + \int_0^{z_i} \left(A + \frac{\partial C}{\partial z} \right) dz + \int_0^{z_i} k_{12b}[PAN](1 - f_{PAN}) dz \right) \tag{17}$$

Figure S21 shows the vertical profiles of various components of this equation. The observed PAN flux is negative and changes slope in the lower half of the CBL, denoting a shift in the equilibrium towards net PAN production at cooler temperatures. This is also reflected in the PAN loss flux (the third term in Eqn. (17)) and is consistent with a previous tower-based analysis of PAN fluxes [*Wolfe et al.*, 2009]. The advection and storage terms also contribute to the total flux. Summing these terms at the flux observation heights gives an estimate for the flux due to primary PA production. Finally, a linear fit of this production flux yields a primary PA production rate of 0.056 pptv s^{-1}. For comparison, *LaFranchi et al.* [2009] estimated a PA production rate of ~0.17 pptv s^{-1} directly above a different forest; higher values in the latter study are expected as calculations were done in the surface layer, where VOC concentrations are higher. Inserting the derived PA production rate back into Eqn. (15) and averaging over the boundary layer gives a mean PAN loss rate of 0.006 pptv s^{-1}, to which we assign a conservative uncertainty of ±50%. Thus, on average, PAN is a source of NO_x in this environment.

In theory, the ground intercept of the fit to the production flux should yield the surface deposition flux, as we did not account for this process at the outset. The estimated ground flux corresponds to a PAN deposition velocity of 1.9 cm s^{-1}, roughly a factor of 2 to 3 higher than what is expected based on resistance considerations and previous observations [*Turnipseed et al.*, 2006; *Wolfe et al.*, 2009]. The difference likely stems from the linear extrapolation of the CBL temperature profile to the surface. Local air temperatures within the canopy may be higher than assumed, implying an under-prediction of the PAN chemical loss flux in this region.

S4.6 Isoprene Oxidation Products

S4.6.1 Production

Attack of isoprene by OH (R1) produces one of eight potential $ISOPO_2$ isomers. These radicals encounter one of several fates, including reactions with NO, HO_2, other RO_2 and isomerization.

$ISOPO_2 + NO \rightarrow 0.117\ ISOPN + 0.883\ (ISOPO + NO_2)$ (R16)

$ISOPO_2 + HO_2 \rightarrow 0.937\ ISOPOOH + 0.063\ (MVK/MACR + HCHO + HO_2)$ (R17)

$ISOPO_2 + RO_2 \rightarrow$ products (R18)

$ISOPO_2 \rightarrow HPALD + HO_2$ (R19)

$ISOPO_2 \rightarrow MVK/MACR + HCHO + OH$ (R20)

Isoprene hydroxynitrates (ISOPN) are a minor product of the reaction with NO, and we adopt here the bulk yield of 11.7% from recent lab studies [*Paulot et al.*, 2009a]. The major alkoxy radicals products (ISOPO) rapidly decompose to carbonyl-containing compounds. Isoprene hydroxyhydroperoxides (ISOPOOH) are the major product of reaction with HO_2, while a minor channel produces carbonyls (methyl vinyl ketone (MVK), methacrolein (MACR), formaldehyde (HCHO)) and HO_2 [*Liu et al.*, 2013]. Reaction with other RO_2 produces numerous multi-functional compounds and is typically slow under most ambient conditions. Recent theoretical [*da Silva et al.*, 2010; *Peeters and Müller*, 2010; *Peeters et al.*, 2009; *Peeters et al.*, 2014] and experimental [*Crounse et al.*, 2011; *Fuchs et al.*, 2013] work has also identified two potential isomerization pathways, both involving auto-oxidation of peroxy radicals. The 1,6 H-shift produces hydroperoxyaldehydes (HPALD) and HO_2, while the 1,5 H-shift produces carbonyls and OH. The bulk rate of the former (i.e. considering the distribution of $ISOPO_2$ isomers) is ~6 times faster than the latter at 295K [*Crounse et al.*, 2011; *da Silva et al.*, 2010], thus we only consider the 1,6 H-shift here. An additional pathway for the 1,6 H-shift, which does not lead to HPALD, has also

recently been proposed [*Peeters et al.*, 2014]; for lack of experimental confirmation, we do not consider this pathway here.

The production rates for ISOPN, ISOPOOH and HPALD are determined by 1) assuming that reaction of isoprene with OH is rate-limiting, and 2) calculating the effective yield for each reaction, α, which is the ratio of the individual reaction rate to the total $ISOPO_2$ loss rate. For example, for ISOPN:

$$\alpha_{ISOPN} = \frac{0.117 k_{16}[NO]}{k_{16}[NO] + k_{17}[HO_2] + k_{18}[RO_2] + k_{19}} \tag{18}$$

$$P_{ISOPN} = k_1[OH][ISOP]\alpha_{ISOPN} \tag{19}$$

This calculation is performed in a vertically-resolved fashion as described below. Calculated CBL-average effective yields and production rates are listed in Table S5. The CBL-average $ISOPO_2$ lifetime is 43 s, with percentage losses due to reactions with NO, HO_2, RO_2 and isomerization of 43%, 43%, 6% and 8%, respectively.

S4.6.2 Loss

Daytime gas-phase losses for oxidation products include oxidation by OH and O_3 and photolysis. Total CBL-average loss rates are given in Table S5. Specific reactions are listed in Table S4 and described further here.

HPALD: Rate constants for reaction of HPALD with OH and O_3 are taken from *Wolfe et al.* [2012], who measured these rates in the laboratory for a functionally similar compound. The HPALD photolysis frequency is derived using the measured value for MACR and assuming a quantum yield of 1 [*Peeters and Müller*, 2010; *Wolfe et al.*, 2012].

ISOPOOH and IEPOX: Reaction of ISOPOOH with OH produces isoprene hydroxyepoxides (IEPOX) with a yield of ~92% [*Paulot et al.*, 2009b]. Because these two compounds are measured as a sum, we only consider the fraction of ISOPOOH oxidation that does not make IEPOX. For ISOPOOH, we use the bulk OH reaction rate constant from *Paulot et al.* [2009b], and the photolysis frequency is assumed equal to that for methyl hydrogen peroxide as recommended by *Saunders et al.* [2003]. IEPOX loss coefficients for reaction with OH were recently quantified in the lab [*Bates et al.*, 2014] and vary between the three isomers. We calculate an isomer-weighted bulk rate coefficient using modeled concentrations of IEPOX isomers from the 0-D box model base simulation (see Sect. 7.2). Reactions of ISOPOOH and IEPOX with O_3 are assumed slow compared to OH reaction. Concentrations of ISOPOOH and IEPOX are estimated by scaling the sum measurement (from the Caltech time-of-flight mass spectrometer) with the fractional distribution observed from slower speciated measurements of these compounds (from the Caltech triple quadrupole mass spectrometer) [*St. Clair et al.*, 2010]. The latter measurements indicate that 78% of the total is ISOPOOH and 22% is IEPOX.

ISOPN: Rate constants for oxidation of ISOPN by OH and O_3 have so far only been measured for three of the eight potential isomers [*L Lee et al.*, 2014]. Isomer-weighted bulk rate coefficients are estimated using modeled concentrations of four representative ISOPN isomers from the 0-D box model base simulation (see Sect. S7.2). The photolysis frequency is assumed equal to that for ethyl nitrate [*Saunders et al.*, 2003].

S4.6.3 Net Chemical Flux Profile

Production and loss rates for HPALD, ISOPOOH + IEPOX and ISOPN are calculated on a 1 m vertical grid ranging from 20 m (the assumed canopy-top height) to 1100 m (the top of the CBL). Profiles for chemical concentrations (NO, O_3, isoprene and oVOC) and meteorological variables (T, P and H_2O) are averaged for each flight segment and interpolated over the observation altitudes. Below the lowest altitude (311 m), meteorological variables are linearly extrapolated based on the CBL profiles while chemical mixing ratios are held constant to average values for the lowest leg. OH and HO_2 concentrations are assumed constant and equal to those derived from isoprene and H_2O_2 flux profiles, respectively. The total RO_2 mixing ratio is estimated by scaling the flux-derived HO_2 concentration by the RO_2/HO_2 ratio (1.55) from the 0-D UWCM base simulation. Photolysis frequencies are averaged over all four flight segments. The chemical flux for $oVOC_i$ is calculated as the cumulative vertical integral of chemical rates:

$$F_Q(z) = \int_{z_0}^{z} \left(\alpha k_1 [OH][ISOP] - \left(k_i [OH] + k_i [O_3] + j_i\right)[oVOC]_i\right) dz \qquad (20)$$

S4.6.4 Analysis of "Missing" Fluxes

Missing fluxes for isoprene oVOC are calculated at each of the four measurement altitudes using mass balance (i.e., the vertically-resolved analogy to Eqn. (2) in the main text).

$$F_{miss}(z) = F_{meas}(z) - F_Q(z) + F_S(z) + F_A(z) \qquad (21)$$

The last two terms in the above equation are the fluxes due to storage and advection, calculated as the ground-up cumulative integral of storage and advection rates (assumed constant) over the CBL. Finally, linear fits to the missing fluxes give deposition fluxes (intercepts) and "missing" loss rates (slopes).

S4.6.5 Heterogeneous Loss

For ISOPOOH + IEPOX and ISOPN, we derive an upper limit for a reactive uptake coefficient, γ, assuming that any "missing" flux is due to this neglected sink. The first-order loss rate for reactive uptake is

$$L_{het} = k_{het}[oVOC] = \left(\frac{r_p}{D} + \frac{4}{\omega\gamma}\right)^{-1} S_p [oVOC] \qquad (22)$$

Here, D is the gas-phase diffusion coefficient (0.106 and 0.095 $cm^2\ s^{-1}$ for IEPOX and ISOPN, respectively), ω is mean molecular speed (230 and 206 m s^{-1} for IEPOX and ISOPN, respectively), and r_p and S_p are the mean particle diameter and surface area, respectively.

While the DC-8 payload included various measurements of particle physical properties, none of the size measurements are performed under ambient humidity conditions. Thus, we use the following method to estimate total particle volume:

1. Integrated particle volumes from the NOAA ultra-high sensitivity aerosol size spectrometer (humidified size distributions) and the NASA scanning mobility particle sizer (dry size distributions)

are averaged over all four flight segments. The difference between dry and wet volumes is taken as the volume of liquid water on the humidified particles.

2. The E-AIM Aerosol Thermodynamics Model II [*Clegg et al.*, 1998; *Wexler and Clegg*, 2002] (available at http://www.aim.env.uea.ac.uk/aim/aim.php) is used to estimate particle liquid water content at ambient relative humidity (65%) and at that of the humidified size measurements (90.77%). Inputs for this model (mass concentrations of NH_4^+, SO_4^{2-} and NO_3^-) are taken from UC-Boulder aerosol mass spectrometer observations averaged over all flight segments. Note that these measurements do not discriminate between "organic" and "inorganic" (i.e. salt) ions.
3. The ratio of AIM-calculated liquid water content at 90.77% and 65% RH is used to scale down the "humid" water volume from the first step. This amount is then added to the dry volume to yield the total particle volume at ambient RH (V_p).

The volume per particle is then estimated by dividing by the average particle number density (N_p = 1856 cm^{-3}), and the radius and surface area are calculated assuming spherical particles. This procedure gives a volume-average particle radius of 77 nm and surface area of 138 m^2 cm^{-3}. Given the coarseness of this method, we assign a conservative uncertainty of ± 50% to these values.

Finally, reactive uptake coefficients are calculated by inverting Eqn. (22) and setting the loss rate equal to the "missing" flux divergence. In this case we assume that all of the loss of ISOPOOH + IEPOX is due only to IEPOX, thus we use the IEPOX concentration as derived in Sect. 3.6.2. Flux-derived uptake coefficients are 0.001 ± 0.004 for IEPOX and 0.023 ± 0.011 for ISOPN.

For comparison, we also estimate γ(IEPOX) using the parameterization of *Gaston et al.* [2014].

$$\frac{1}{\gamma} = \frac{r_p \omega}{4D} + \frac{1}{\alpha_p} + \frac{1}{\Gamma_{aq}} \tag{23}$$

$$\Gamma_{aq} = \frac{4V_p RTH_{aq} k_{aq}}{S_p \omega} \tag{24}$$

$$k_{aq} = k_{H+}\left[H^+\right] + k_{nuc}[nuc]a_{H+} + k_{ga}[ga] \tag{25}$$

Here, α_p is the mass accommodation coefficient (0.1), R is the universal gas constant, T is average CBL temperature (294.2 K), H_{aq} is the IEPOX Henry's Law coefficient (1.7 x 10^8 M atm^{-1}) [*Gaston et al.*, 2014], k_{H+} is the rate constant for acid-catalyzed ring opening (0.036 M^{-1} s^{-1}) [*Cole-Filipiak et al.*, 2010], $[H^+]$ is proton concentration, a_{H+} is proton activity (taken from AIM-II model output), k_{nuc} is the rate constant for reaction with nucleophiles (2 x 10^{-4} M^{-1} s^{-1}) [*Eddingsaas et al.*, 2010], *[nuc]* is the concentration of nucleophiles (sulfate and nitrate), k_{ga} is the rate constant for reaction with general acids (7.3 x 10^{-4} M^{-1} s^{-1}) [*Eddingsaas et al.*, 2010], and *[ga]* is the concentration of general acids (bisulfate). Aerosol-phase ion concentrations are taken from the AIM II model as described above, which gives an aerosol pH of 0.21. The IEPOX uptake coefficient estimated by this method is 0.037 ± 0.030. Using a lower value for H_{aq} (3 x 10^7 M atm^{-1}) as recommended by *McNeill et al.* [2012] reduces the parameterized γ to 0.010 ± 0.006.

S5. Entrainment Velocity

The entrainment velocity (v_e) describes the rate of air exchange between the boundary layer and free troposphere (or, equivalently, the boundary layer growth rate) and is parameterized as

$$v_e = \frac{F(z_i)}{C_{BL} - C_{FT}} \tag{26}$$

Here, $F(z_i)$ is the flux at the top of the boundary layer and C_{BL} and C_{FT} are the mean scalar values in the boundary layer and free troposphere, respectively. For fluxes exhibiting a linear or near-linear vertical profile, we calculate the entrainment flux by evaluating the linear least-squares fits at the boundary layer height of 1060 m. Boundary layer concentrations are the average of measurements from the third flight segment, and free troposphere concentrations are a 2-minute average of observations taken at 1200-1300 m directly after the fourth flight leg. Figure S22 shows entrainment velocities as calculated from fluxes of potential temperature (sensible heat), isoprene, H_2O_2, O_3, NO_x, ISOPOOH+IEPOX and ISOPN. Isoprene and ozone fluxes give comparable entrainment velocities (4.8 and 5.1 cm s^{-1}, respectively), while v_e derived from other species are biased low. This can occur if the BL-FT concentration difference is small relative to the absolute magnitude of concentrations, resulting in large uncertainties (i.e. H_2O_2, NO_x, ISOPN). In essence, we cannot determine the concentration difference with sufficient precision for these compounds. For T and ISOPOOH+IEPOX, the reason for disagreement is less clear; the only significant distinction for these species is that storage comprises a significant fraction of the budget equation, though this is also true for ozone (Table S2). Regardless, the strength of isoprene fluxes and the strong concentration difference (~4.8 ppbv in the boundary layer and essential zero in the free troposphere) provides confidence that v_e derived from this measurement is the most accurate.

S6. Resistance Parameterization

We employ a standard resistance model [*Wesely*, 1989] to estimate the deposition velocity of H_2O_2 in the limit of no surface resistance. In analogy to an electrical circuit, this model assumes that a molecule must pass through a series of "resistances," which represent physical processes, before being deposited to a surface. These processes include: 1) turbulent transport from the CBL to the surface, represented by the aerodynamic resistance (R_a), 2) molecular diffusion through a viscous layer of air immediately above the surface, represented by the laminar sublayer resistance (R_b), and 3) actual physical or reactive loss at the surface, represented by the surface resistance (R_c). The units for resistance are inverse velocity, and adding these processes in series gives the deposition velocity (v_d).

$$v_d = \left(\frac{1}{R_a + R_b + R_c} \right)^{-1} \tag{27}$$

R_c is often further decomposed into resistances for various processes (e.g. uptake by plant stomata vs. deposition on plant cuticles), which are parameterized according to the effective Henry's law coefficient and a semi-physical "reactivity" factor. Here we examine only the limiting case where $R_c \approx 0$, implying that a molecule is lost as soon as it reaches the surface.

The aerodynamic resistance is calculated from standard equations that depend on atmospheric stability [*Arya*, 1988; *Seinfeld and Pandis*, 2006]. For this calculation we use an estimated canopy height of 20 m, a displacement height of 15 m and a roughness length of 1.5 m. The Obukhov length of -29 m (calculated from extrapolated surface potential temperature and momentum fluxes) indicates moderately unstable boundary layer, consistent with the observed lapse rate of 8 K km^{-1}. The aerodynamic resistance determined from this approach is 7.1 s m^{-1}.

The laminar sublayer resistance is calculated for a forest canopy following *Jensen and Hummelshøj* [1995] and *Jensen and Hummelshøj* [1997]:

$$R_b = \frac{\nu}{u^* D}\left(\frac{cu^* l}{\nu LAI^2}\right)^{1/3} \quad (28)$$

The friction velocity (u*) is 0.39 m s^{-1} based on extrapolated momentum fluxes (not shown). The kinematic viscosity for air (ν) is 0.15 cm^2 s^{-1}. The diffusion coefficient for H_2O_2 (*D*) is 0.19 cm^2 s^{-1}. The leaf area index (LAI) is taken as 6.9 m^2 m^{-2} based on the NLDAS product (Fig. S2B). The tunable constant, *c*, is set to its nominal value of 100. The "typical leaf width," *l*, represents the scale of individual drag elements. For a coniferous forest this is the width of a pine needle (0.1 cm). For mixed and deciduous forests this parameter is not well-defined, thus we choose a reasonable range of 0.5 to 1 cm. This gives a range of 13.1 to 16.5 s m^{-1} for R_b.

Returning to Eqn. (27), we calculate an upper limit H_2O_2 deposition velocity of 4.2 to 5.0 cm s^{-1}.

S7. Model Descriptions

7.1 GEOS-Chem

We compare our surface flux estimates to the state-of-the-science GEOS-Chem global chemical transport model (version 9-02, http://geos-chem.org), originally described by *Bey et al.* [2001] and *Park et al.* [2004]. GEOS-Chem is driven by Goddard Earth Observing System (GEOS-FP) assimilated meteorological data from the NASA Global Modeling and Assimilation Office (GMAO). The GEOS-FP meteorological data have a native horizontal resolution of 0.25° x 0.3125° with 72 vertical pressure levels and 3 h temporal frequency (1 h for surface variables and mixing depths).

The model simulation was done at the native GEOS-FP resolution and includes detailed isoprene, oxidant, and aerosol chemistry as described in *Mao et al.* [2013]. Biogenic VOC emissions are calculated online using the Model of Emissions of Gases and Aerosols from Nature (MEGAN 2.1) inventory of *Guenther et al.* [2012]. NO_x emissions include contributions from soil and fertilizer sources [*Hudman et al.*, 2012]. Dry deposition is based on the resistance-in-series scheme of *Wesely* [1989] as implemented in GEOS-Chem by *Wang et al.* [1998].

S7.2 UWCM

Box model calculations for HO_x and isoprene-derived oVOC are carried out using the University of Washington Chemical Model (UWCM) v2.2. This model is based on a more complex 1-D model [*Wolfe and Thornton*, 2011] and has been used previously to simulate HO_x in other forested environments [*Kim et al.*, 2013; *Wolfe et al.*, 2014]. Core chemistry utilizes the Master Chemical Mechanism (MCM) v3.2 [*Jenkin et al.*, 1997; *Saunders et al.*, 2003] with isoprene and methane as initial VOC. The mechanism has been updated to reflect results of recent lab studies, including:

1. OH and ozone reaction rate constants for ISOPN and IEPOX [*L Lee et al.*, 2014],
2. yields of second-generation isoprene nitrates [*Paulot et al.*, 2009a],
3. OH reaction rates and products for glycoaldehyde [*Butkovskaya et al.*, 2006] and methylglyoxal [*Baeza-Romero et al.*, 2007], and
4. $ISOPO_2$ inter-conversion and isomerization and subsequent chemistry [*Peeters and Müller*, 2010; *Peeters et al.*, 2009; *Peeters et al.*, 2014] using the explicit mechanism of *Archibald et al.* [2010] with rate constants for the 1,6 and 1,5 H-shifts following *Crounse et al.* [2011] and*da Silva et al.* [2010], respectively.

An additional physical loss lifetime of 24 hours is also assumed for all species to simulate dilution, deposition and other physical losses not explicitly modeled. This is a necessary step to circumvent unrealistic build-up of long-lived oxidation products.

Simulations are performed for measurements along the first three flux segments. The model is constrained with 10-second mean observations of O_3, NO_2, H_2O_2, isoprene, HCHO, MVK, MACR, PAN, temperature, pressure, relative humidity, location and time. Concentrations of CH_4, H_2 and CO are set to constant values of 1800 ppb, 550 ppb and 152 ppb, respectively. A scaling factor for model-calculated photolysis frequencies (to account for, e.g., cloud cover) is calculated as the ratio of measured to modeled $J(NO_2)$. For each set of 10-second mean observations, the model is integrated forward using a solar cycle with a time step of 1 hour and a total integration time of 72 hours, which is sufficient for species of interest to reach steady state. Photolysis frequencies and NO concentrations are allowed to respond to solar forcing, while other gas and meteorological variables listed above are held fixed at their observed values.

In addition to the base simulation described above, we perform simulations to test the sensitivity of modeled HO_x concentrations to several key processes. Each of these tests are done with respect to the base case, and results are listed in Table S6. In simulation M1, the rate constant for the 1,6 H-shift of certain $ISOPO_2$ radicals to produce HPALD is increased to the most recent theoretical recommendation [*Peeters et al.*, 2014]. In simulation M2, the rate constant for the reaction of isoprene with OH is reduced by an upper limit of 50% [*Butler et al.*, 2008] to mimic the effects of reactant segregation, which may occur when the timescale for loss of a reactant (in this case OH) is much slower than the turbulent mixing timescale [*Krol et al.*, 2000]. In simulations M3a-b, the physical loss rate constant (inverse of the loss lifetime) is reduced or increased by a factor of 2, respectively. It has been shown previously that assumptions about this rate can significantly affect modeled OH reactivity [*Edwards et al.*, 2013], but in the present case the effects on HO_x concentrations are minimal (Table S6).

S8 References

Archibald, A. T., M. C. Cooke, S. R. Utembe, D. E. Shallcross, R. G. Derwent, and M. E. Jenkin (2010), Impacts of mechanistic changes on HOx formation and recycling in the oxidation of isoprene, *Atmos. Chem. Phys.*, *10*, 8097-8118.

Arya, S. P. (1988), *Introduction to Micrometeorology*, Academic Press, San Diego, CA.

Atkinson, R., D. Baulch, R. Cox, J. Crowley, R. Hampson, R. Hynes, M. Jenkin, M. Rossi, and J. Troe (2004), Evaluated kinetic and photochemical data for atmospheric chemistry: Volume I - gas phase reactions of O-x, HOx, NOx and SOx species, *Atmos. Chem. Phys.*, *4*, 1461-1738.

Atkinson, R., D. Baulch, R. Cox, J. Crowley, R. Hampson, R. Hynes, M. Jenkin, M. Rossi, and J. Troe (2006), Evaluated kinetic and photochemical data for atmospheric chemistry: Volume II - gas phase reactions of organic species, *Atmos. Chem. Phys.*, *6*, 3625-4055.

Baeza-Romero, M. T., D. R. Glowacki, M. A. Blitz, D. E. Heard, M. J. Pilling, A. R. Rickard, and P. W. Seakins (2007), A combined experimental and theoretical study of the reaction between methylglyoxal and OH/OD radical: OH regeneration, *Phys. Chem. Chem. Phys.*, *9*(31), 4114-4128.

Bates, K., J. Crounse, J. St Clair, N. Bennett, T. Nguyen, J. Seinfeld, B. Stoltz, and P. Wennberg (2014), Gas Phase Production and Loss of Isoprene Epoxydiols, *J. Phys. Chem. A*, *118*(7), 1237-1246.

Bey, I., D. J. Jacob, R. M. Yantosca, J. A. Logan, B. D. Field, A. M. Fiore, Q. B. Li, H. G. Y. Liu, L. J. Mickley, and M. G. Schultz (2001), Global modeling of tropospheric chemistry with assimilated meteorology: Model description and evaluation, *J. Geophys. Res. Atmos.*, *106*(D19), 23073-23095.

Butkovskaya, N. I., N. Pouvesle, A. Kukui, and G. Le Bra (2006), Mechanism of the OH-initiated oxidation of glycolaldehyde over the temperature range 233-296 K, *J. Phys. Chem. A*, *110*(50), 13492-13499.

Butler, T., D. Taraborrelli, C. Fischer, H. Harder, M. Martinez, J. Williams, M. Lawrence, and J. Lelieveld (2008), Improved simulation of isoprene oxidation chemistry with the ECHAM5/MESSy chemistry-climate model: lessons from the GABRIEL airborne field campaign, *Atmos. Chem. Phys.*, *8*(16), 4529-4546.

Cazorla, M., G. M. Wolfe, S. A. Bailey, A. K. Swanson, H. L. Arkinson, and T. F. Hanisco (2015), A new airborne laser-induced fluorescence instrument for in situ detection of Formaldehyde throughout the troposphere and lower stratosphere, *Atmos. Meas. Tech.*, *8*, 541-552.

Chan, K., J. Dean-Day, S. Bowen, and T. Bui (1998), Turbulence measurements by the DC-8 meteorological measurement system, *Geophys. Res. Lett.*, *25*(9), 1355-1358.
Clegg, S., P. Brimblecombe, and A. Wexler (1998), Thermodynamic model of the system H+-NH4+-SO42--NO3--H2O at tropospheric temperatures, *J. Phys. Chem. A*, *102*(12), 2137-2154.
Cole-Filipiak, N., A. O'Connor, and M. Elrod (2010), Kinetics of the Hydrolysis of Atmospherically Relevant Isoprene-Derived Hydroxy Epoxides, *Env. Sci. Technol.*, *44*(17), 6718-6723.
Crounse, J. D., K. A. McKinney, A. J. Kwan, and P. O. Wennberg (2006), Measurement of gas-phase hydroperoxides by chemical ionization mass spectrometry, *Anal. Chem.*, *78*(19), 6726-6732.
Crounse, J. D., F. Paulot, H. G. Kjaergaard, and P. O. Wennberg (2011), Peroxy radical isomerization in the oxidation of isoprene, *Phys. Chem. Chem. Phys.*, *13*(30), 13607-13613.
da Silva, G., C. Graham, and Z. F. Wang (2010), Unimolecular beta-Hydroxyperoxy Radical Decomposition with OH Recycling in the Photochemical Oxidation of Isoprene, *Env. Sci. Technol.*, *44*(1), 250-256.
de Gouw, J., and C. Warneke (2007), Measurements of volatile organic compounds in the earths atmosphere using proton-transfer-reaction mass spectrometry, *Mass Spec. Rev.*, *26*(2), 223-257.
DiGangi, J. P., et al. (2011), First direct measurements of formaldehyde flux via eddy covariance: implications for missing in-canopy formaldehyde sources, *Atmos. Chem. Phys.*, *11*, 10565-10578.
Eddingsaas, N., D. VanderVelde, and P. Wennberg (2010), Kinetics and Products of the Acid-Catalyzed Ring-Opening of Atmospherically Relevant Butyl Epoxy Alcohols, *J. Phys. Chem. A*, *114*(31), 8106-8113.
Edwards, P. M., et al. (2013), OH reactivity in a South East Asian tropical rainforest during the Oxidant and Particle Photochemical Processes (OP3) project, *Atmos. Chem. Phys.*, *13*(18), 9497-9514.
Farmer, D. K., and R. C. Cohen (2008), Observations of HNO3, SAN, SPN and NO2 fluxes: evidence for rapid HOx chemistry within a pine forest canopy, *Atmos. Chem. Phys.*, *8*, 3899-3917.
Fuchs, H., et al. (2013), Experimental evidence for efficient hydroxyl radical regeneration in isoprene oxidation, *Nature Geosci.*, *6*(12), 1023-1026.
Gaston, C. J., T. P. Riedel, Z. Zhang, A. Gold, J. D. Surratt, and J. A. Thornton (2014), Reactive Uptake of an Isoprene-derived Epoxydiol to Submicron Aerosol Particles, *Env. Sci. Technol.*, *48*, 11178-11186.
Guenther, A. B., X. Jiang, C. L. Heald, T. Sakulyanontvittaya, T. Duhl, L. K. Emmons, and X. Wang (2012), The Model of Emissions of Gases and Aerosols from Nature version 2.1 (MEGAN2.1): an extended and updated framework for modeling biogenic emissions, *Geosci. Mod. Dev.*, *5*, 1471-1492.
Hudman, R. C., N. E. Moore, A. K. Mebust, R. V. Martin, A. R. Russell, L. C. Valin, and R. C. Cohen (2012), Steps towards a mechanistic model of global soil nitric oxide emissions: implementation and space based-constraints, *Atmos. Chem. Phys.*, *12*(16), 7779-7795.
Jenkin, M. E., S. M. Saunders, and M. J. Pilling (1997), The tropospheric degradation of volatile organic compounds: A protocol for mechanism development, *Atmos. Env.*, *31*(1), 81-104.
Jensen, N. O., and P. Hummelshøj (1995), Derivation of canopy resistance for water vapour fluxes over a spruce forest, using a new technique for the viscous sublayer resistance, *Agr. Forest Met.*, *73*, 339-352.
Jensen, N. O., and P. Hummelshøj (1997), Erratum to "Derivation of canopy resistance for water vapor fluxes over a spruce forest, using a new technique for the viscous sublayer resistance", *Agr. Forest Met.*, *85*, 289.
Jimenez, J., et al. (2003), Ambient aerosol sampling using the Aerodyne Aerosol Mass Spectrometer, *J. Geophys. Res. Atmos.*, *108*(D7).
Kaimal, J. C., y. Izumi, J. C. Wyngaard, and R. Cote (1972), Spectral characteristics of surface-layer turbulence, *Quarterly Journal of the Royal Meteorological Society*, *98*(417), 563-&.
Karl, T., P. Misztal, H. Jonsson, S. Shertz, A. Goldstein, and A. Guenther (2013), Airborne Flux Measurements of BVOCs above Californian Oak Forests: Experimental Investigation of Surface and Entrainment Fluxes, OH Densities, and Damkohler Numbers, *J. Atmos. Sci.*, *70*(10), 3277-3287.
Kim, S., et al. (2013), Evaluation of HOx sources and cycling using measurement-constrained model calculations in a 2-methyl-3-butene-2-ol (MBO) and monoterpene (MT) dominated ecosystem, *Atmos. Chem. Phys.*, *13*(4), 2031-2044.

Krol, M. C., M. J. Molemaker, and J. V. G. de Arellano (2000), Effects of turbulence and heterogeneous emissions on photochemically active species in the convective boundary layer, *J. Geophys. Res. Atmos.*, *105*(D5), 6871-6884.

LaFranchi, B. W., et al. (2009), Closing the peroxy acetyl nitrate budget: observations of acyl peroxy nitrates (PAN, PPN, and MPAN) during BEARPEX 2007, *Atmos. Chem. Phys.*, *9*, 7623-7641.

Lee, L., A. P. Teng, P. O. Wennberg, J. D. Crounse, and R. C. Cohen (2014), On Rates and Mechanisms of OH and O-3 Reactions with Isoprene-Derived Hydroxy Nitrates, *J. Phys. Chem. A*, *118*(9), 1622-1637.

Lee, X., W. Massman, and B. Law (2004), *Handbook of Micrometeorology: A Guide for Surface Flux Measurement and Analysis*, Kluwer Academic Publishers, Dordrecht, The Netherlands.

Lenschow, D. H., and L. Kristensen (1986), Sampling errors in flux measurements of slowly depositing pollutants, *Journal of Climate and Applied Meteorology*, *25*(11), 1785-1787.

Lenschow, D. H., J. Mann, and L. Kristensen (1994), How long is long enough when measuring fluxes and other turbulence statistics, *J. Atmos. Ocean. Technol.*, *11*(3), 661-673.

Liu, Y. J., I. Herdlinger-Blatt, K. A. McKinney, and S. T. Martin (2013), Production of methyl vinyl ketone and methacrolein via the hydroperoxyl pathway of isoprene oxidation, *Atmos. Chem. Phys.*, *13*(11), 5715-5730.

Mao, J., F. Paulot, D. J. Jacob, R. c. Cohen, J. D. Crounse, P. O. Wennberg, C. A. Keller, R. C. Hudman, M. P. Barkley, and L. W. Horowitz (2013), Ozone and organic nitrates over the eastern United States: Sensitivity to isoprene chemistry, *J. Geophys. Res.*, *118*(11), 11256-11268.

Mauder, M., R. Desjardins, and I. MacPherson (2007), Scale analysis of airborne flux measurements over heterogeneous terrain in a boreal ecosystem, *J. Geophys. Res. Atmos.*, *112*(D13).

Mauder, M., M. Cuntz, C. Drue, A. Graf, C. Rebmann, H. Schmid, M. Schmidt, and R. Steinbrecher (2013), A strategy for quality and uncertainty assessment of long-term eddy-covariance measurements, *Agr. Forest Met.*, *169*, 122-135.

McNeill, V. F., J. L. Woo, D. D. Kim, A. N. Schwier, N. J. Wannell, A. J. Sumner, and J. M. Barakat (2012), Aqueous-Phase Secondary Organic Aerosol and Organosulfate Formation in Atmospheric Aerosols: A Modeling Study, *Env. Sci. Technol.*, *46*(15), 8075-8081.

Misztal, P. K., T. Karl, R. Weber, H. H. Jonsson, A. B. Guenther, and A. H. Goldstein (2014), Airborne flux measurements of biogenic volatile organic compounds over California, *Atmos. Chem. Phys.*, *14*, 10631-10647.

Park, R. J., D. J. Jacob, B. D. Field, R. M. Yantosca, and M. Chin (2004), Natural and transboundary pollution influences on sulfate-nitrate-ammonium aerosols in the United States: Implications for policy, *J. Geophys. Res. Atmos.*, *109*(D15).

Paulot, F., J. D. Crounse, H. G. Kjaergaard, J. H. Kroll, J. H. Seinfeld, and P. O. Wennberg (2009a), Isoprene photooxidation: new insights into the production of acids and organic nitrates, *Atmos. Chem. Phys.*, *9*(4), 1479-1501.

Paulot, F., J. D. Crounse, H. G. Kjaergaard, A. Kurten, J. M. St Clair, J. H. Seinfeld, and P. O. Wennberg (2009b), Unexpected Epoxide Formation in the Gas-Phase Photooxidation of Isoprene, *Science*, *325*(5941), 730-733.

Peeters, J., and J. F. Müller (2010), HOx radical regeneration in isoprene oxidation via peroxy radical isomerisations. II: experimental evidence and global impact, *Phys. Chem. Chem. Phys.*, *12*(42), 14227-14235.

Peeters, J., T. L. Nguyen, and L. Vereecken (2009), HOx radical regeneration in the oxidation of isoprene, *Phys. Chem. Chem. Phys.*, *11*(28), 5935-5939.

Peeters, J., J.-F. Muller, T. Stavrakou, and V. S. Nguyen (2014), Hydroxyl Radical Recycling in Isoprene Oxidation Driven by Hydrogen Bonding and Hydrogen Tunneling: The Upgraded LIM1 Mechanism, *J. Phys. Chem. A*, *118*, 8625-8643.

Perring, A. E., et al. (2009), Airborne observations of total RONO2: new constraints on the yield and lifetime of isoprene nitrates, *Atmos. Chem. Phys.*, *9*(4), 1451-1463.

Petropavlovskikh, I., R. Shetter, S. Hall, K. Ullmann, and P. Bhartia (2007), Algorithm for the charge-coupled-device scanning actinic flux spectroradiometer ozone retrieval in support of the Aura satellite validation, *J. Appl. Rem. Sens.*, *1*.

Pollack, I., B. Lerner, and T. Ryerson (2010), Evaluation of ultraviolet light-emitting diodes for detection of atmospheric NO2 by photolysis - chemiluminescence, *J. Atmos. Chem.*, *65*(2-3), 111-125.

Ryerson, T., E. Williams, and F. Fehsenfeld (2000), An efficient photolysis system for fast-response NO2 measurements, *J. Geophys. Res. Atmos.*, *105*(D21), 26447-26461.

Ryerson, T., L. Huey, K. Knapp, J. Neuman, D. Parrish, D. Sueper, and F. Fehsenfeld (1999), Design and initial characterization of an inlet for gas-phase NOy measurements from aircraft, *J. Geophys. Res. Atmos.*, *104*(D5), 5483-5492.

Saunders, S. M., M. E. Jenkin, R. G. Derwent, and M. J. Pilling (2003), Protocol for the development of the Master Chemical Mechanism, MCM v3 (Part A): tropospheric degradation of non-aromatic volatile organic compounds, *Atmos. Chem. Phys.*, *3*, 161-180.

Seinfeld, J. H., and S. N. Pandis (2006), *Atmospheric Chemistry and Physics*, 2nd ed., John Wiley and Sons, Inc., Hoboken, NJ.

Sievers, J., T. Papakyriakou, S. Larsen, M. M. Jammet, S. Rysgaard, M. K. Sejr, and L. L. Sorensen (2015), Estimating surface fluxes using eddy covariance and numerical ogive optimization, *Atmos. Chem. Phys.*, *15*, 2081-2103.

Slusher, D. L., L. G. Huey, D. J. Tanner, F. M. Flocke, and J. M. Roberts (2004), A thermal dissociation-chemical ionization mass spectrometry (TD-CIMS) technique for the simultaneous measurement of peroxyacyl nitrates and dintrogen pentoxide, *J. Geophys. Res.*, *109*(D19315).

Spirig, C., A. Neftel, C. Ammann, J. Dommen, W. Grabmer, A. Thielmann, A. Schaub, J. Beauchamp, A. Wisthaler, and A. Hansel (2005), Eddy covariance flux measurements of biogenic VOCs during ECHO 2003 using proton transfer reaction mass spectrometry, *Atmos. Chem. Phys.*, *5*, 465-481.

St. Clair, J. M., D. C. McCabe, J. D. Crounse, U. Steiner, and P. O. Wennberg (2010), Chemical ionization tandem mass spectrometer for the in situ measurement of methyl hydrogen peroxide, *Rev. Sci. Inst.*, *81*, 094102.

Torrence, C., and G. Compo (1998), A practical guide to wavelet analysis, *Bull. Am. Met. Soc.*, *79*(1), 61-78.

Turnipseed, A. A., L. G. Huey, E. Nemitz, R. Stickel, J. Higgs, D. J. Tanner, D. L. Slusher, J. P. Sparks, F. Flocke, and A. Guenther (2006), Eddy covariance fluxes of peroxyacetyl nitrates (PANs) and NOy to a coniferous forest, *J. Geophys. Res.*, *111*, D09304.

Wang, Y. H., D. J. Jacob, and J. A. Logan (1998), Global simulation of tropospheric O-3-NOx-hydrocarbon chemistry 1. Model formulation, *J. Geophys. Res. Atmos.*, *103*(D9), 10713-10725.

Weil, J. C., T. W. Horst, S. E. Schwartz, and W. G. N. Slinn (1992), Footprint estimates for atmospheric flux measurements in the convective boundary-layer, *Precipitation Scavenging and Atmosphere-Surface Exchange, Vols 1-3*, 717-728.

Wesely, M. L. (1989), Parameterization of surface resistances to gaseous dry deposition in regional-scale numerical models, *Atmos. Env.*, *23*(6), 1293-1304.

Wexler, A., and S. Clegg (2002), Atmospheric aerosol models for systems including the ions H+, NH4+, Na+, SO42-, NO3-,Cl-, Br-, and H2O, *J. Geophys. Res. Atmos.*, *107*(D14).

Wienhold, F. G., H. Frahm, and G. W. Harris (1994), Measurements of n2o fluxes from fertilized grassland using a fast-response tunable diode-laser spectrometer, *J. Geophys. Res. Atmos.*, *99*(D8), 16557-16567.

Wolfe, G. M., and J. A. Thornton (2011), The Chemistry of Atmosphere-Forest Exchange (CAFE) Model - Part 1: Model Description and Characterization, *Atmos. Chem. Phys.*, *11*, 77-101.

Wolfe, G. M., J. A. Thornton, R. L. N. Yatavelli, M. McKay, A. H. Goldstein, B. LaFranchi, K. E. Min, and R. C. Cohen (2009), Eddy covariance fluxes of acyl peroxy nitrates (PAN, PPN and MPAN) above a Ponderosa pine forest, *Atmos. Chem. Phys.*, *9*(2), 615-634.

Wolfe, G. M., J. D. Crounse, J. D. Parrish, J. M. St. Clair, M. R. Beaver, F. Paulot, T. P. Yoon, P. O. Wennberg, and F. N. Keutsch (2012), Photolysis, OH reactivity and ozone reactivity of a proxy for isoprene-derived hydroperoxyenals (HPALDs), *Phys. Chem. Chem. Phys.*, *14*(20), 7276-7286.

Wolfe, G. M., et al. (2014), Missing peroxy radical sources within a summertime ponderosa pine forest, *Atmos. Chem. Phys.*, *14*, 4715-4732.

Wooldridge, P. J., et al. (2010), Total peroxy nitrates (SPNs) in the atmosphere: the thermal dissociation-laser induced fluorescence (TD-LIF) technique and comparisons to speciated PAN measurements, *Atmos. Meas. Tech.*, *3*, 593-607.

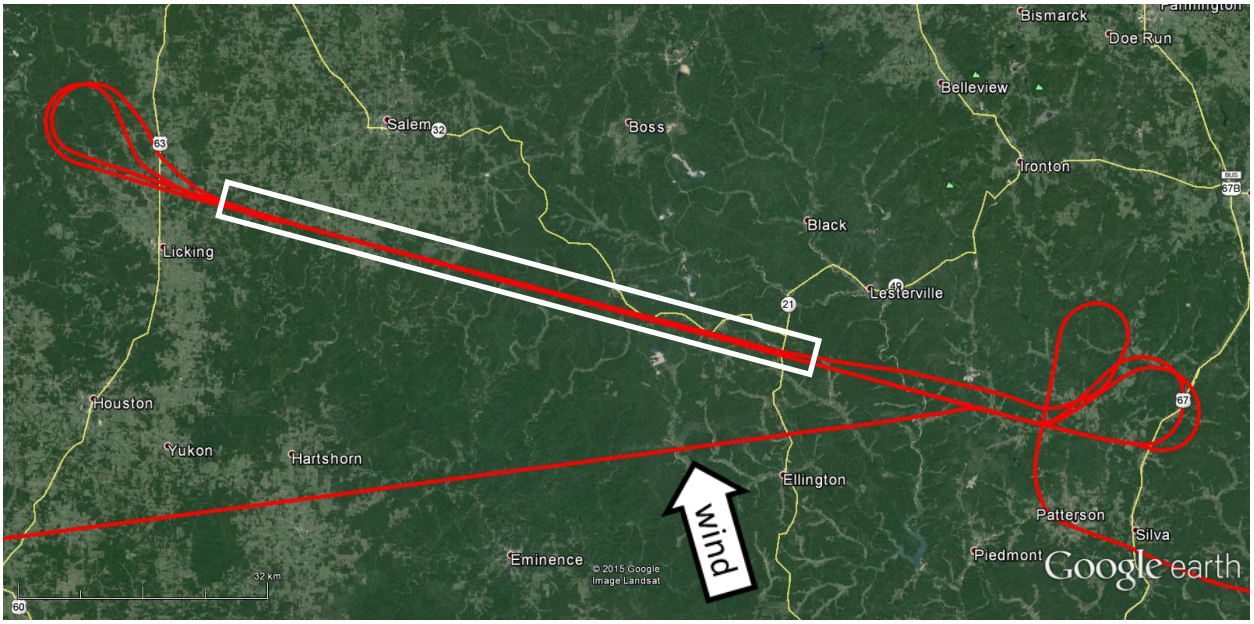

Figure S1. Detailed map of the Ozark Mountains study area. The flight track is shown as a red line. The white box denotes the region of flux calculations, corresponding to the gray boxes in Figs. 2 and S3. Mean wind direction is indicated by the arrow. Yellow lines are state highways.

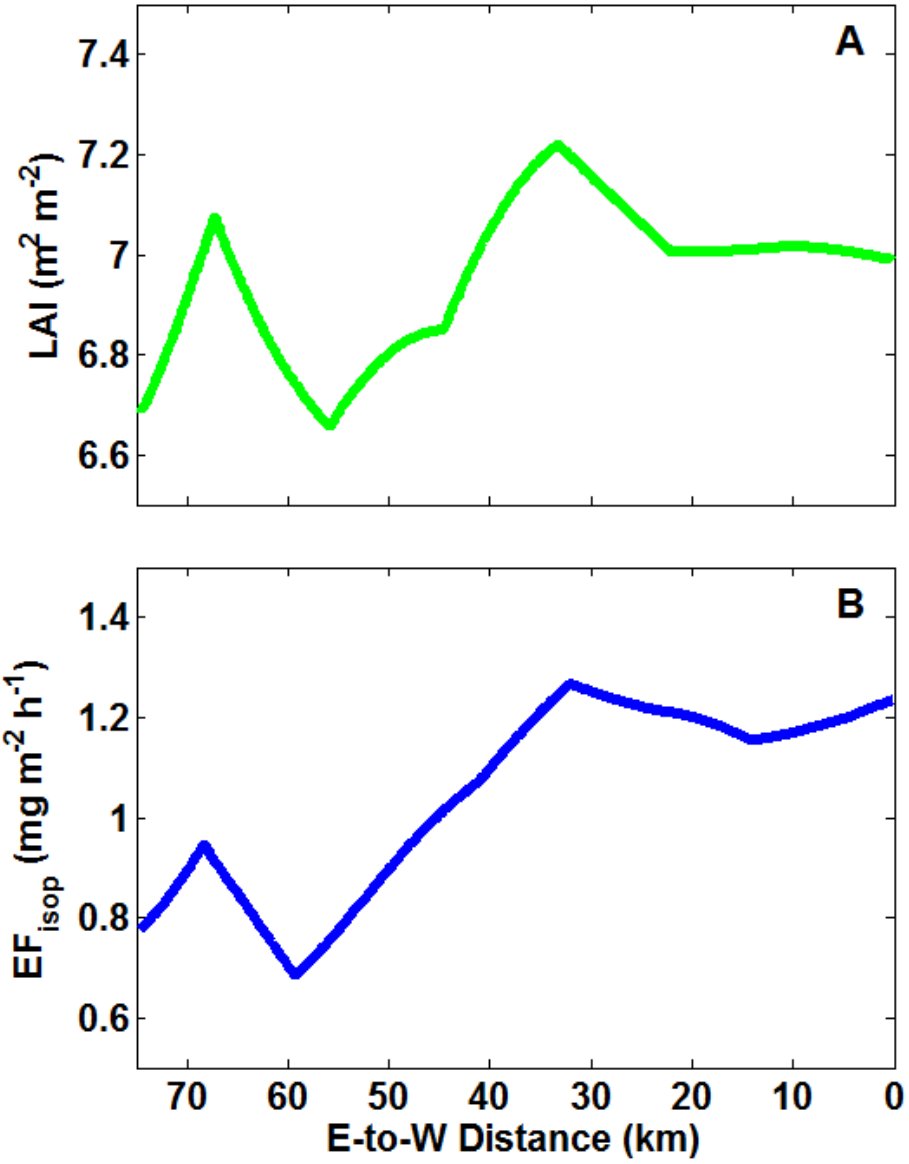

Figure S2. Canopy characteristics along the flight transect. The x-axis for both plots is the same as that used to present wavelet-derived fluxes (e.g. Fig. 3). (A) Leaf area index (leaf area per unit ground area) derived from the Mosaic land surface model (available at http://disc.sci.gsfc.nasa.gov/datacollection/NLDAS_MOS0125_H_V002.html, last accessed 04/09/2015). Model output was obtained for September 06, 2013 on a native 0.125x0.125 degree grid and interpolated to aircraft position along the first flux leg. (B) MEGANv2.1 isoprene emission factors (emission rate per unit leaf area at reference conditions for temperature and insolation). The emission factor map (available at http://lar.wsu.edu/megan/guides.html, last accessed 04/09/2015) was regridded to 0.1x0.1 degrees and interpolated to the aircraft position along the first flight leg.

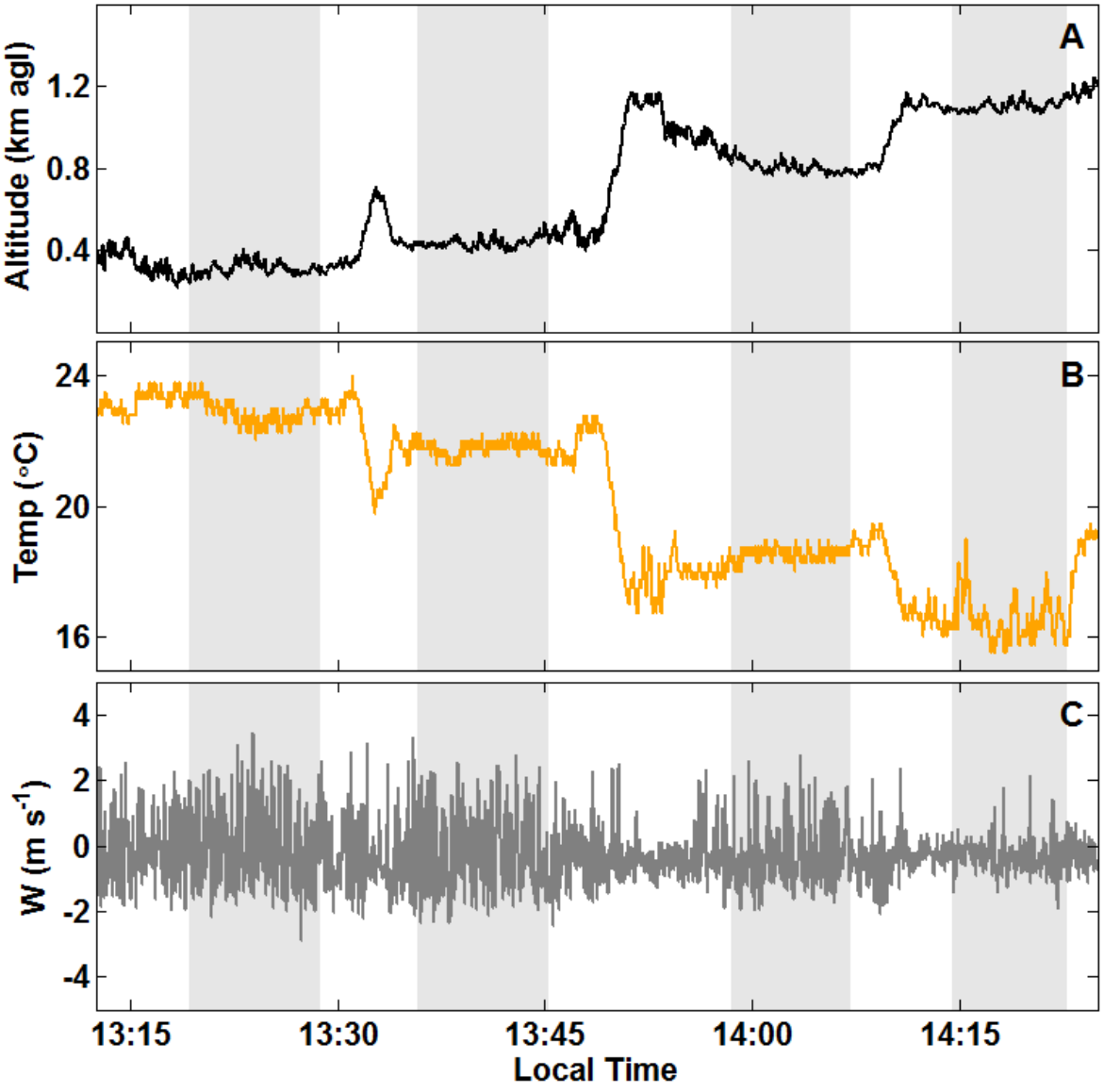

Figure S3. Time series for observations during the Ozarks transects on 06 September 2013. All observations are 1 Hz. Shaded regions denote the segments used for flux calculations. Gaps in some time series are due to normal instrument operation (e.g. signal background measurements). Also see next two pages. Note the logarithmic scale for NO_x (E) and PAN (F).

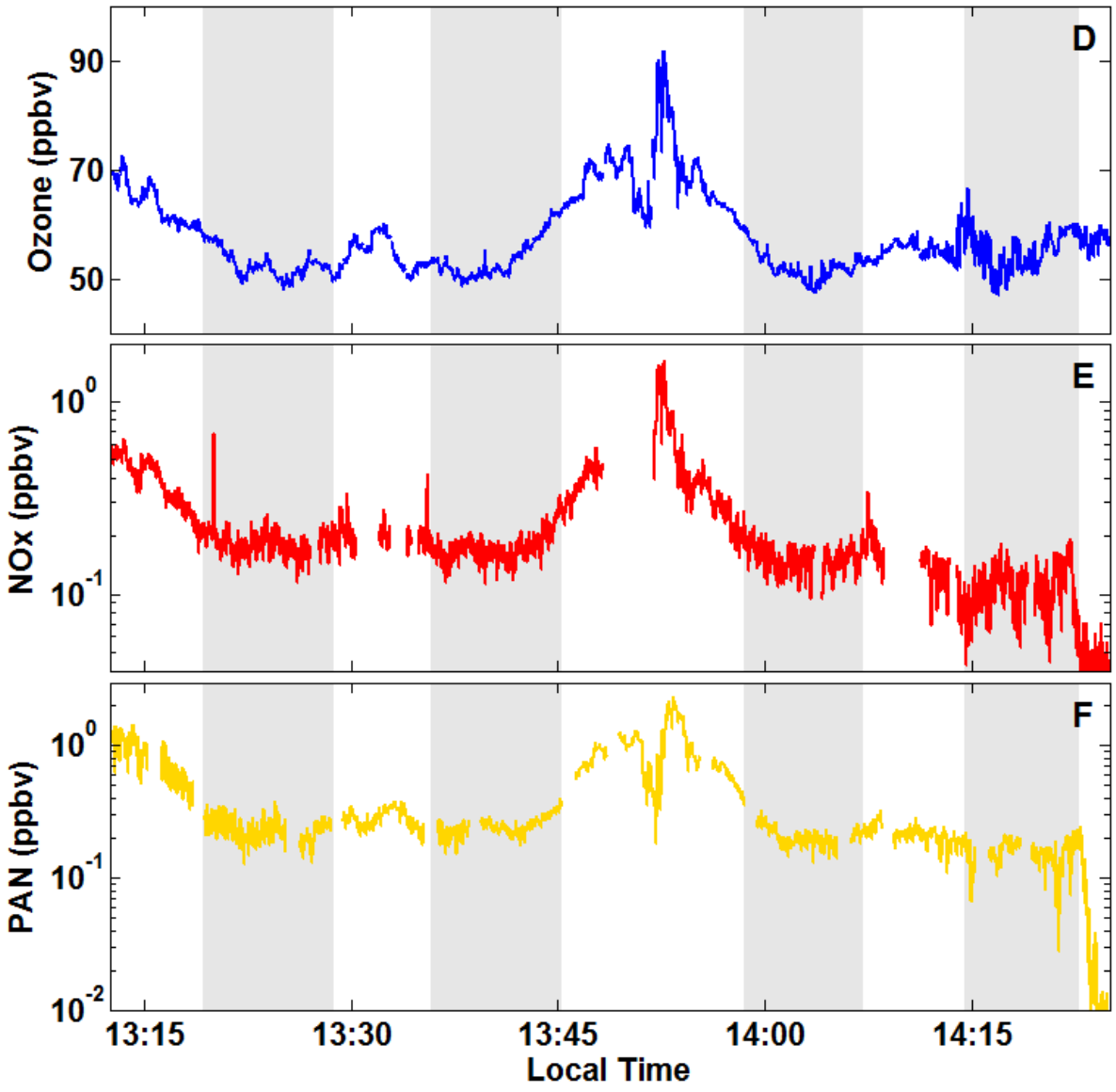

Figure S3. Continued.

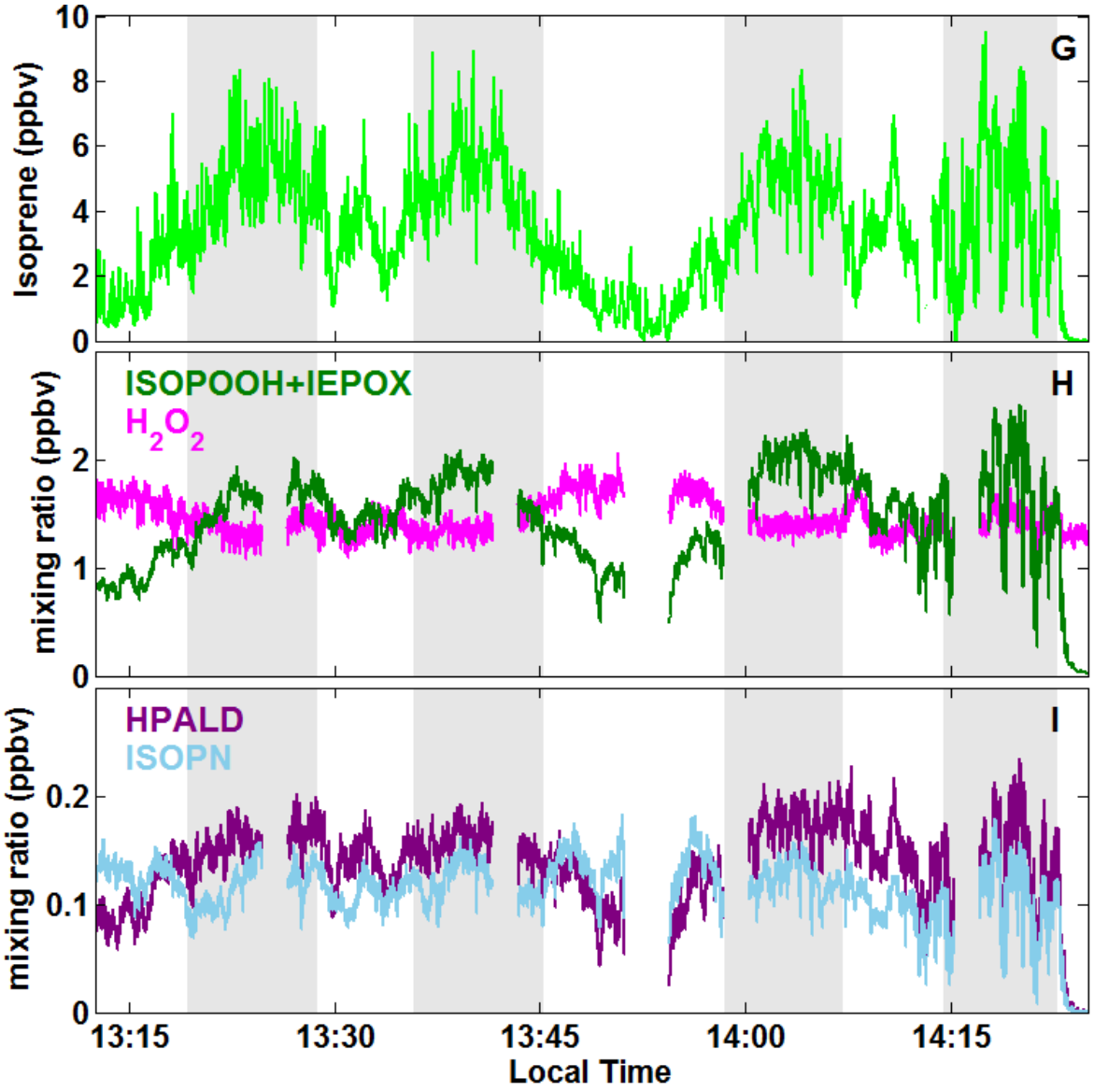

Figure S3. Continued.

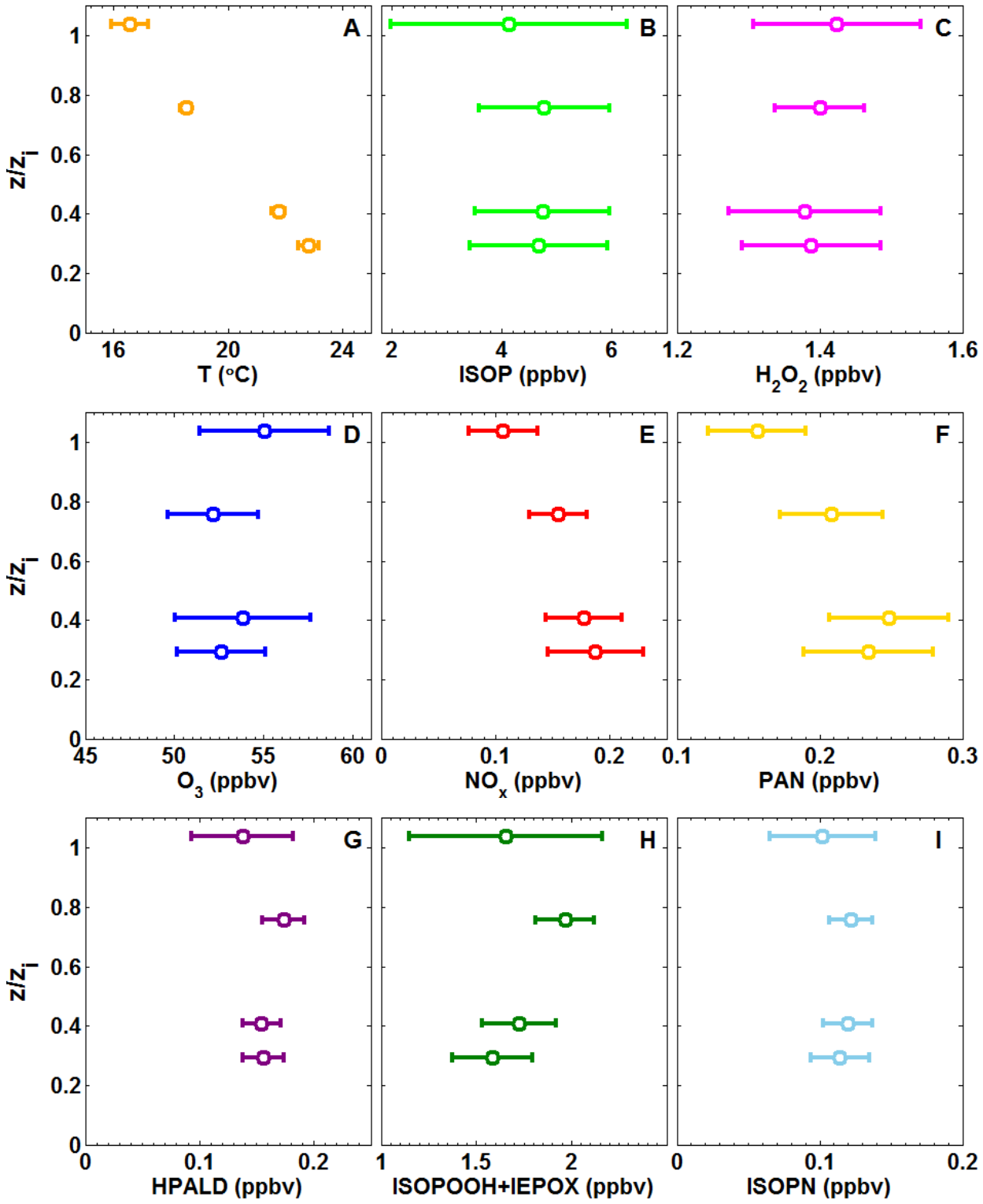

Figure S4. Vertical profiles of observations of the Ozarks. Data are means ± 1σ for each segment highlighted in Fig. S3. The vertical coordinate is normalized by the CBL height of 1060 m.

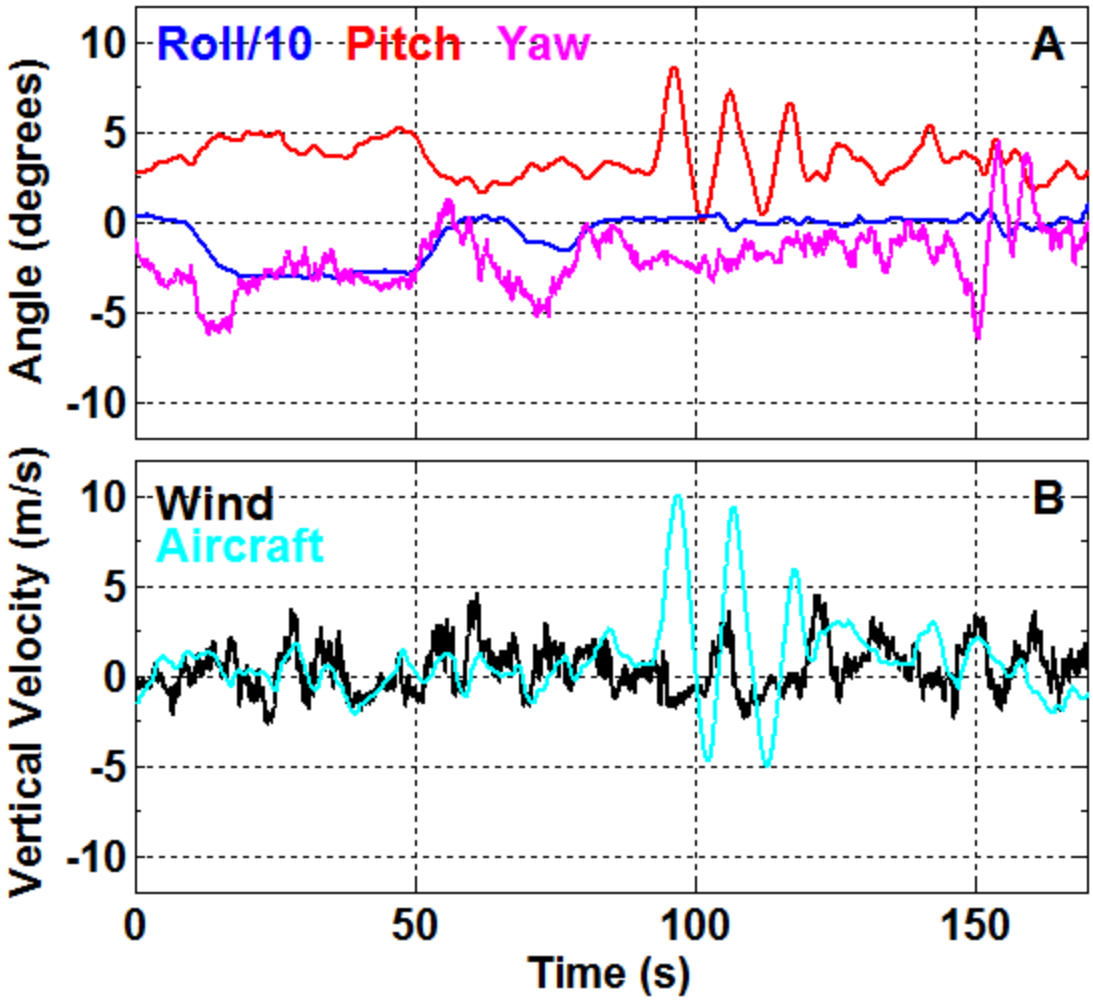

Figure S5. Example of roll, pitch and yaw (sideslip) maneuvers for calibration of vertical wind measurements. Maneuvers were carried out at ~15:30 EST at an altitude of 600 – 800 m. The data indicate no major bleed-through of aircraft motions to the derived vertical wind speed.

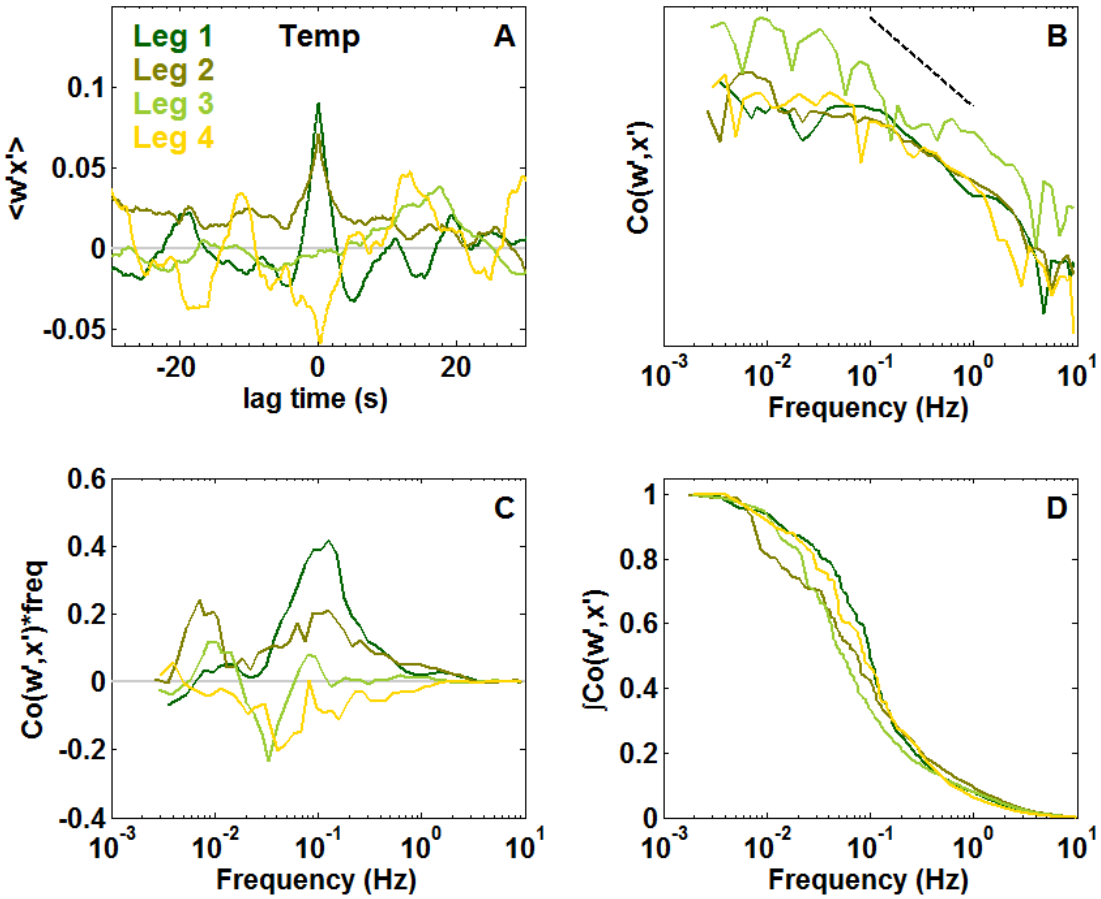

Figure S6. Eddy covariance quality analysis for potential temperature (sensible heat) fluxes. (A) The peaks in the lagged covariance of vertical wind and temperature fluctuations are used to correct for time-shifts before calculation of the total covariance. (B) Cospectra provide a check on the measurement of fluxes throughout the spectral range of CBL turbulence. Curves are normalized to their integrals and averaged into 50 logarithmically-spaced bins. The dashed line represents a theoretical -7/3 slope. (C) Multiplication of cospectra by frequency gives a clearer picture of the relative contributions of different signal frequencies to total covariance. (D) Ogives are the cumulative integral under the cospectra. Ideally, these taper to asymptotes at the high and low frequency ends, indicating that most of the co-spectral power was captured by observations.

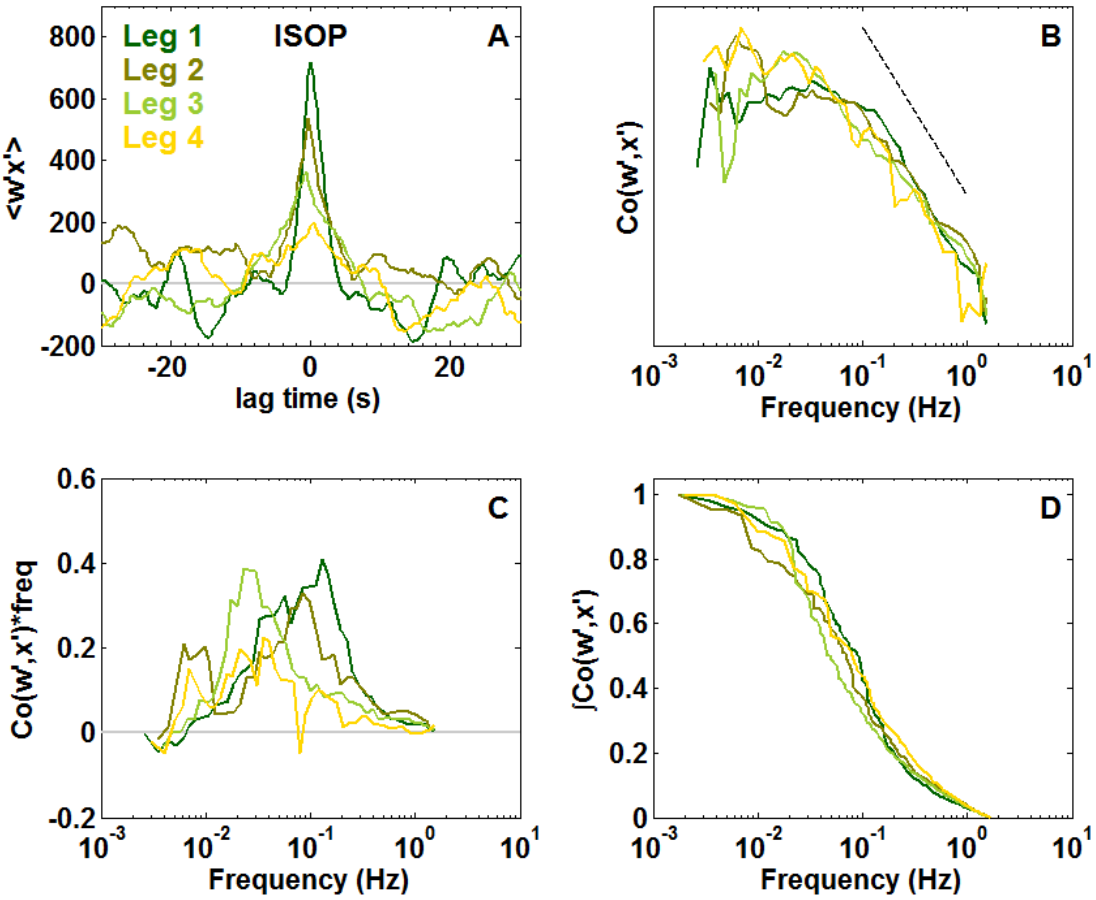

Figure S7. Eddy covariance quality analysis for isoprene fluxes. See Fig. S6 for details.

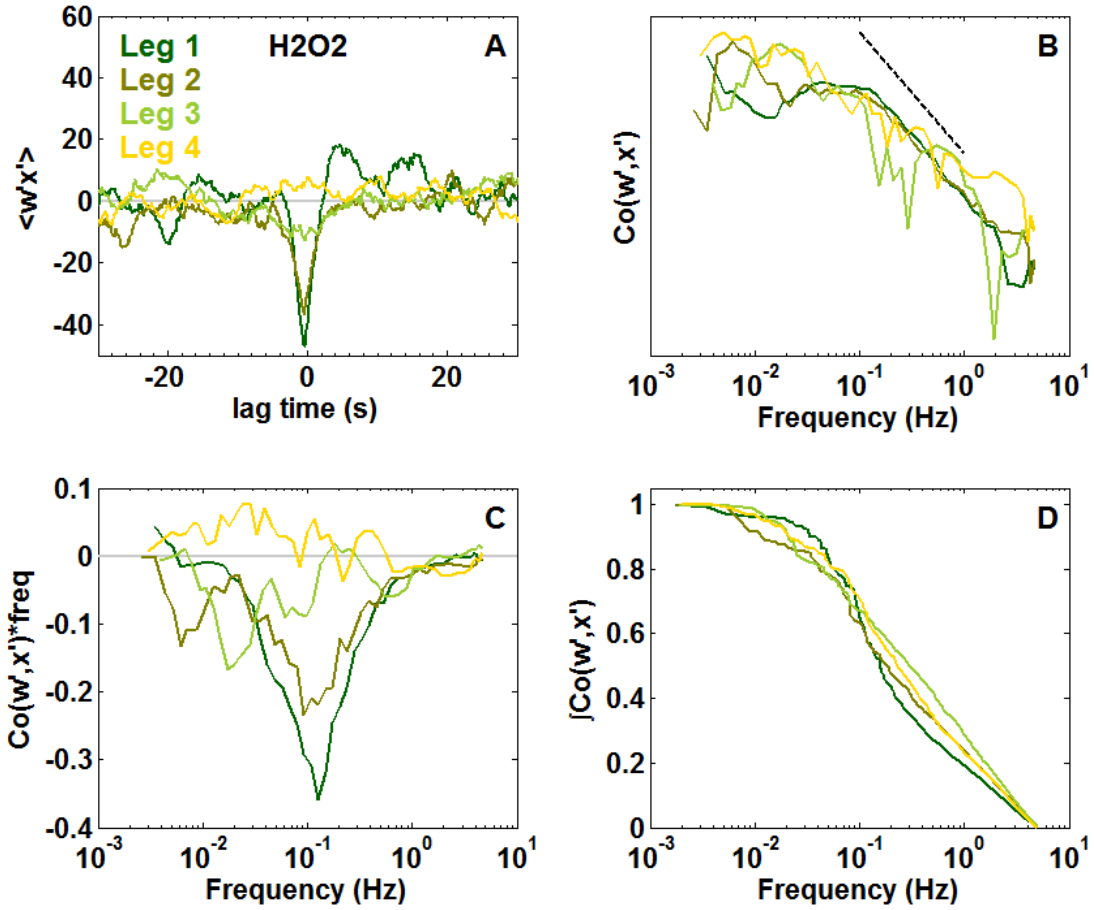

Figure S8. Eddy covariance quality analysis for hydrogen peroxide fluxes. See Fig. S6 for details.

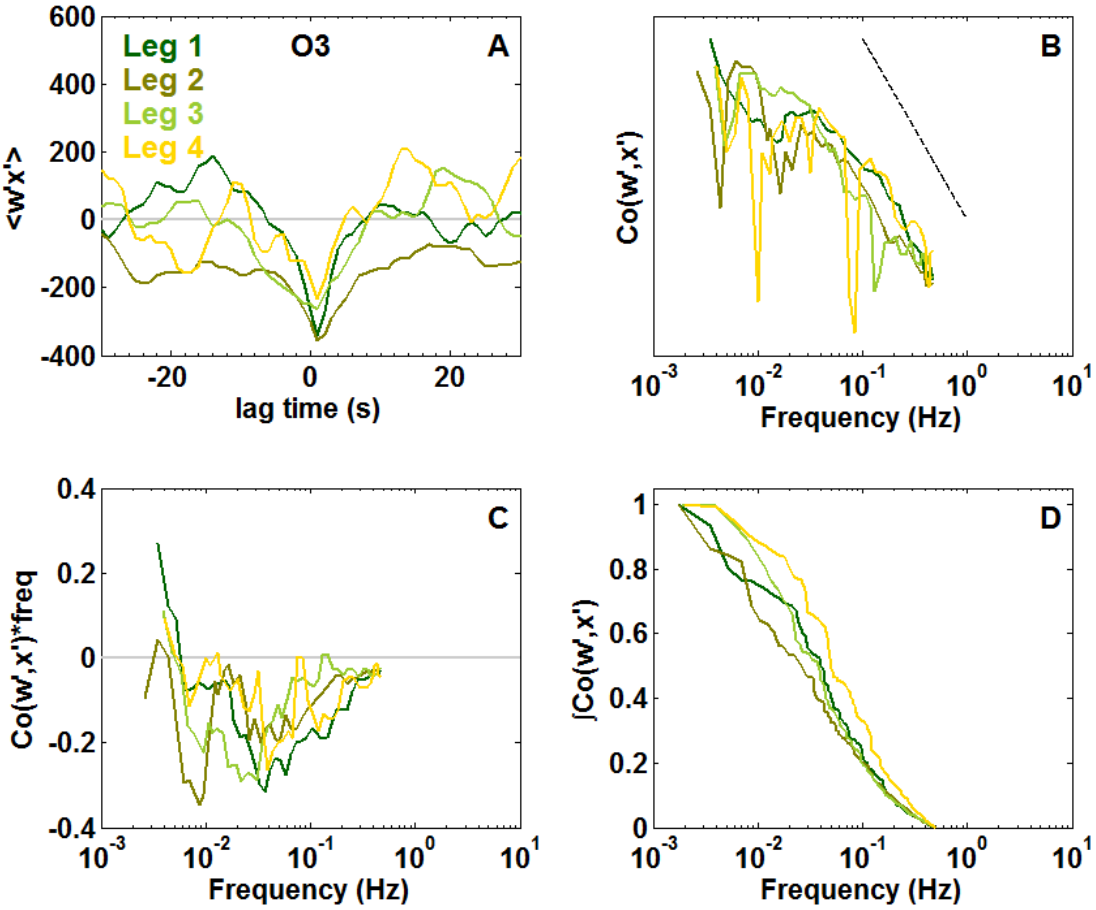

Figure S9. Eddy covariance quality analysis for ozone fluxes. See Fig. S6 for details.

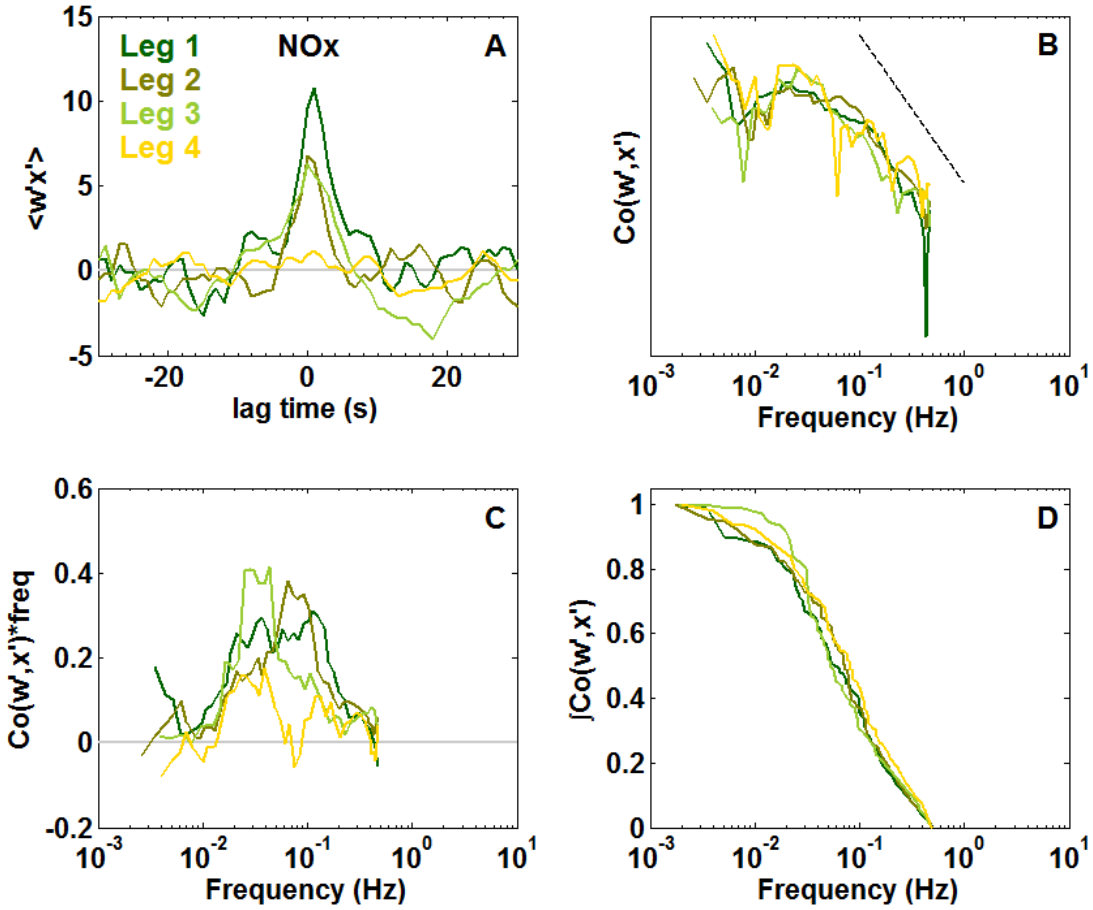

Figure S10. Eddy covariance quality analysis for NOx fluxes. See Fig. S6 for details.

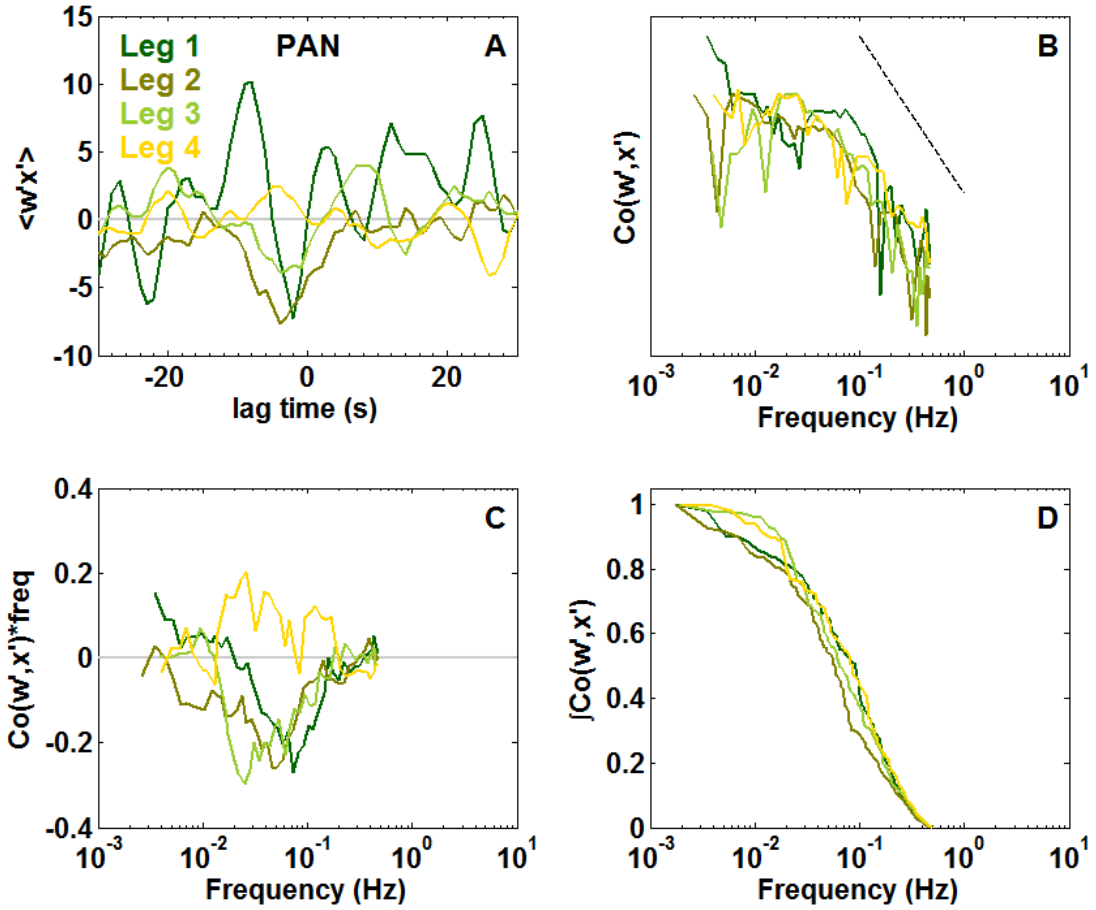

Figure S11. Eddy covariance quality analysis for peroxyacetyl nitrate fluxes. See Fig. S6 for details.

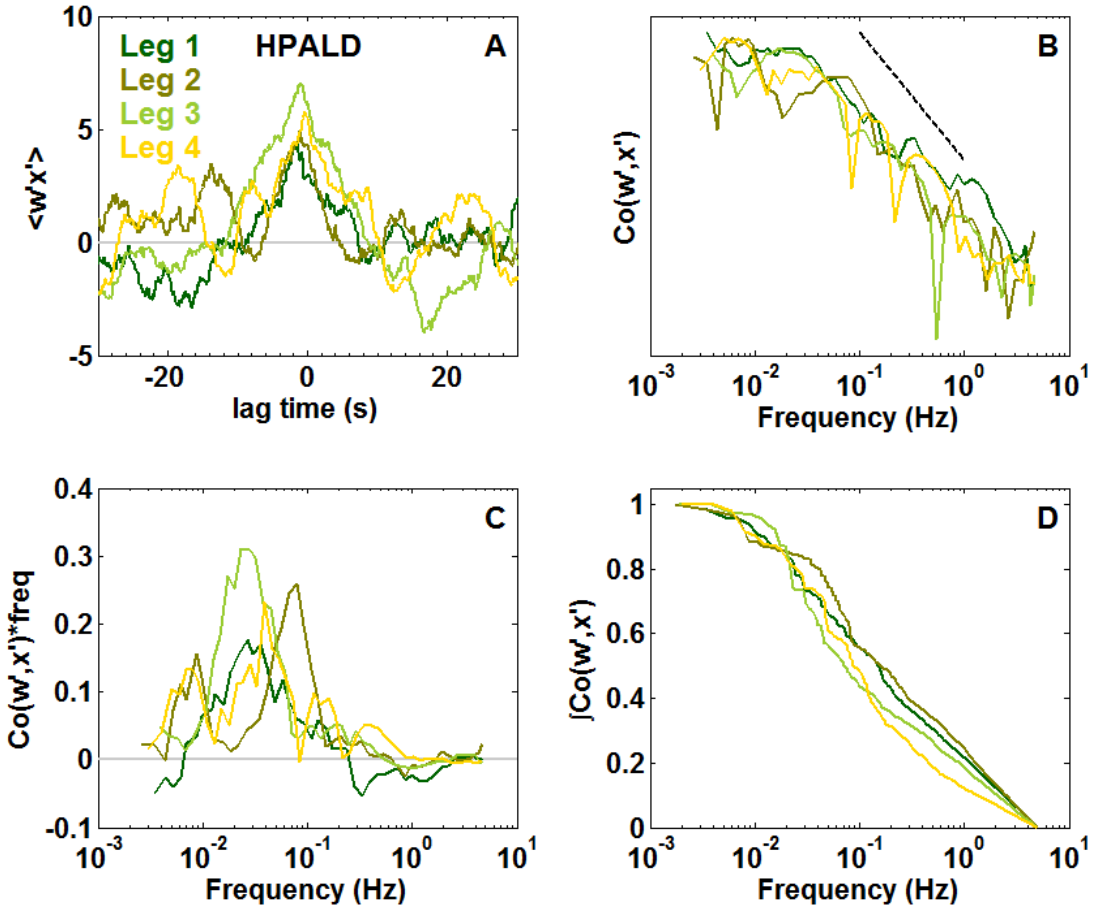

Figure S12. Eddy covariance quality analysis for isoprene-derived HPALD fluxes. See Fig. S6 for details.

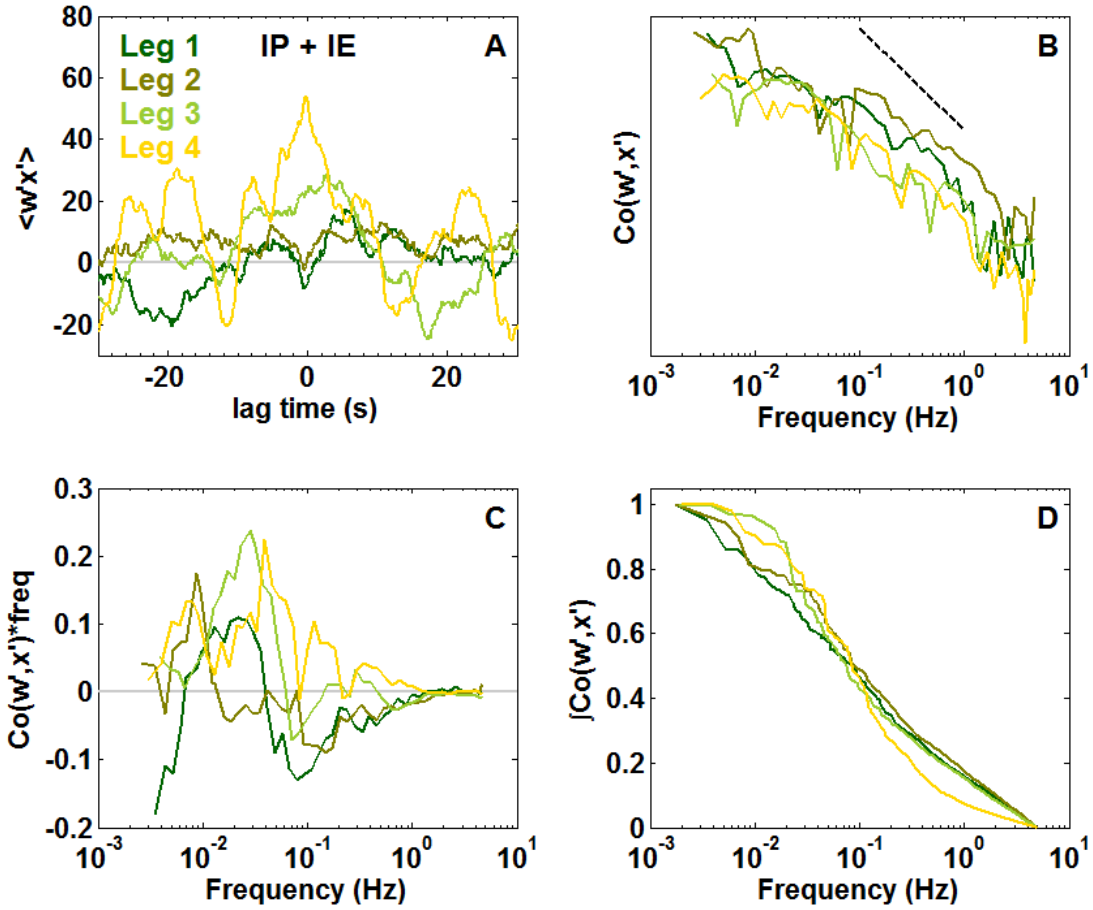

Figure S13. Eddy covariance quality analysis for fluxes of ISOPOOH + IEPOX. See Fig. S6 for details.

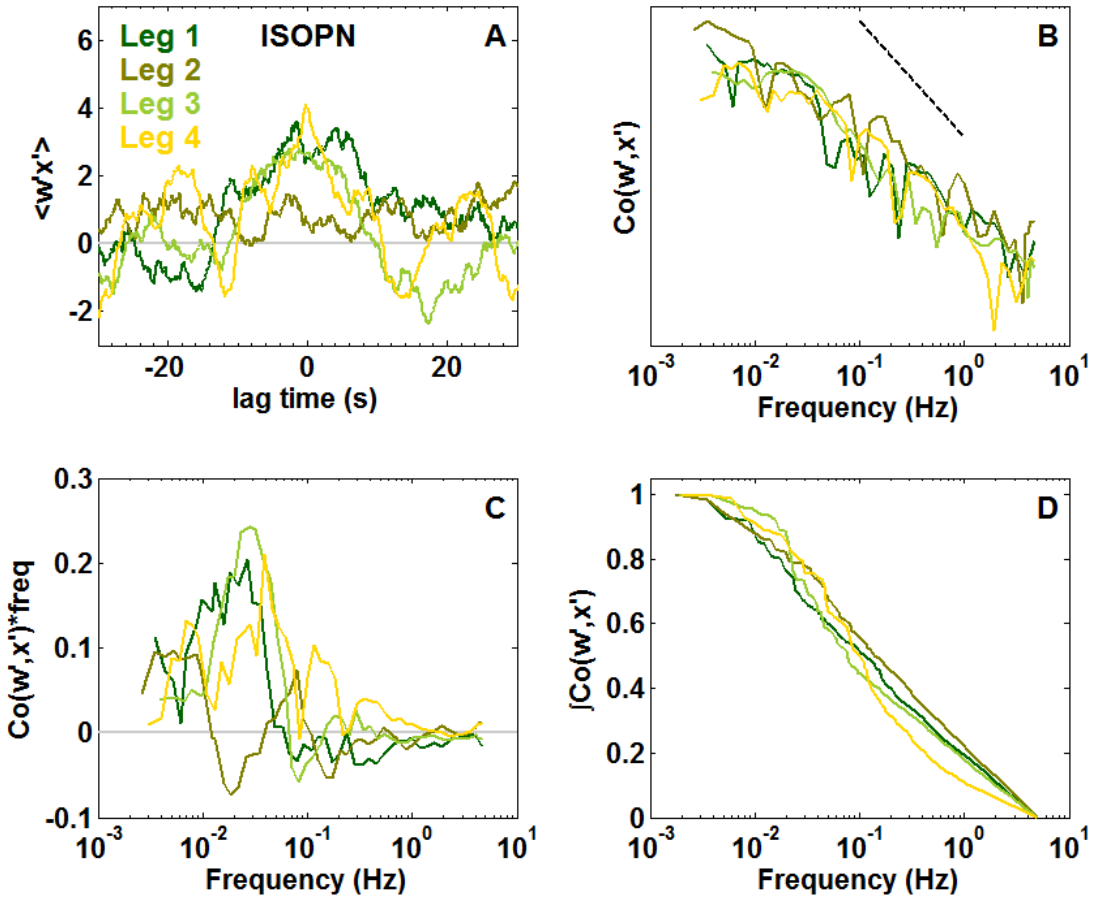

Figure S14. Eddy covariance quality analysis for total ISOPN fluxes. See Fig. S6 for details.

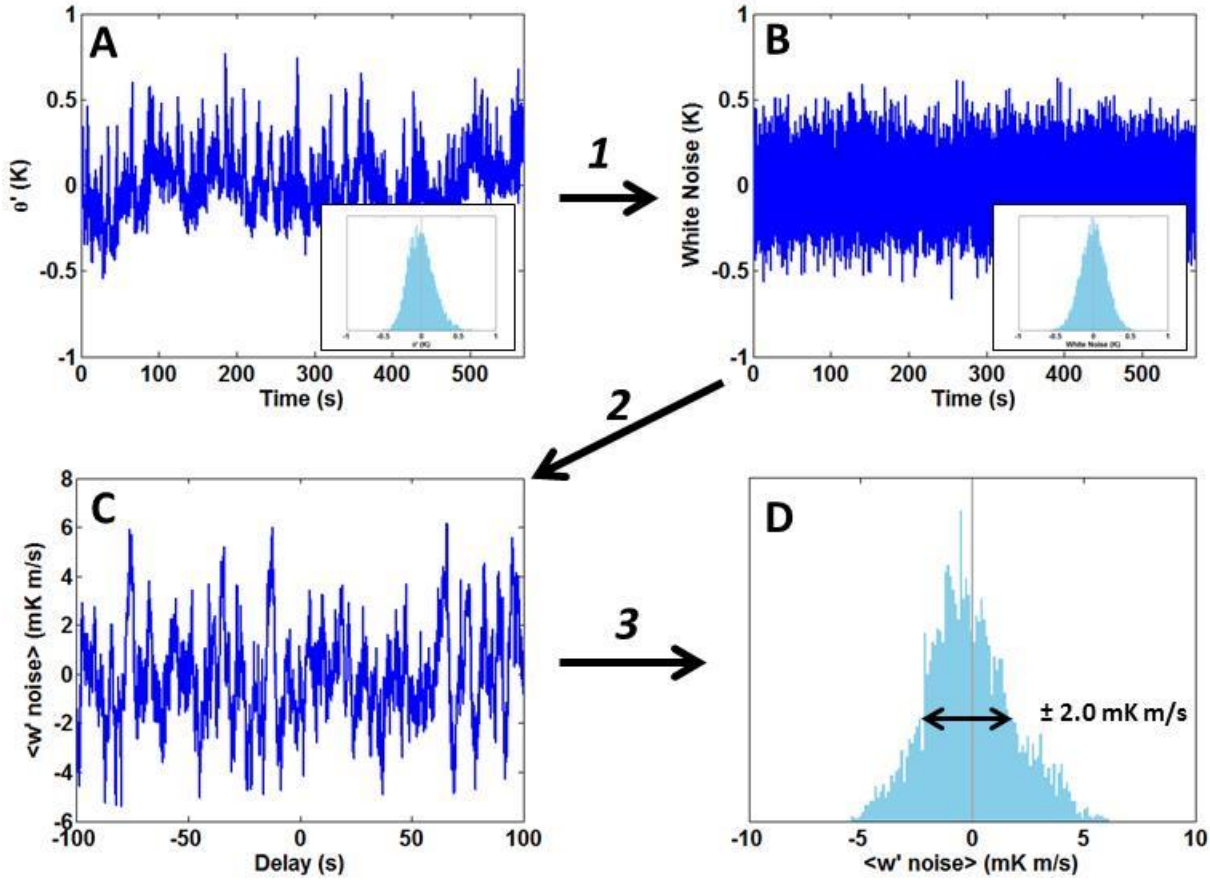

Figure S15. Illustration of a flux detection limit calculation using the noise covariance method. Here we use potential temperature from the first leg as an example. Starting with a despiked and detrended scalar time series (A), a white noise time series is generated with the same mean and standard deviation (B). Insets in (A) and (B) show the frequency distribution for both time series. Next, the covariance of the noise time series with vertical wind velocity (w') is calculated for various time lags (C). Note that there is no clear peak in the covariance versus delay time, unlike when this calculation is done with the actual time series (Fig. S6A). Finally, the standard deviation of the distribution of noise covariance (D) is defined as the 1σ flux detection limit. For this example, the detection limit is 2.0 mK m/s, and the actual flux is 88 mK m/s.

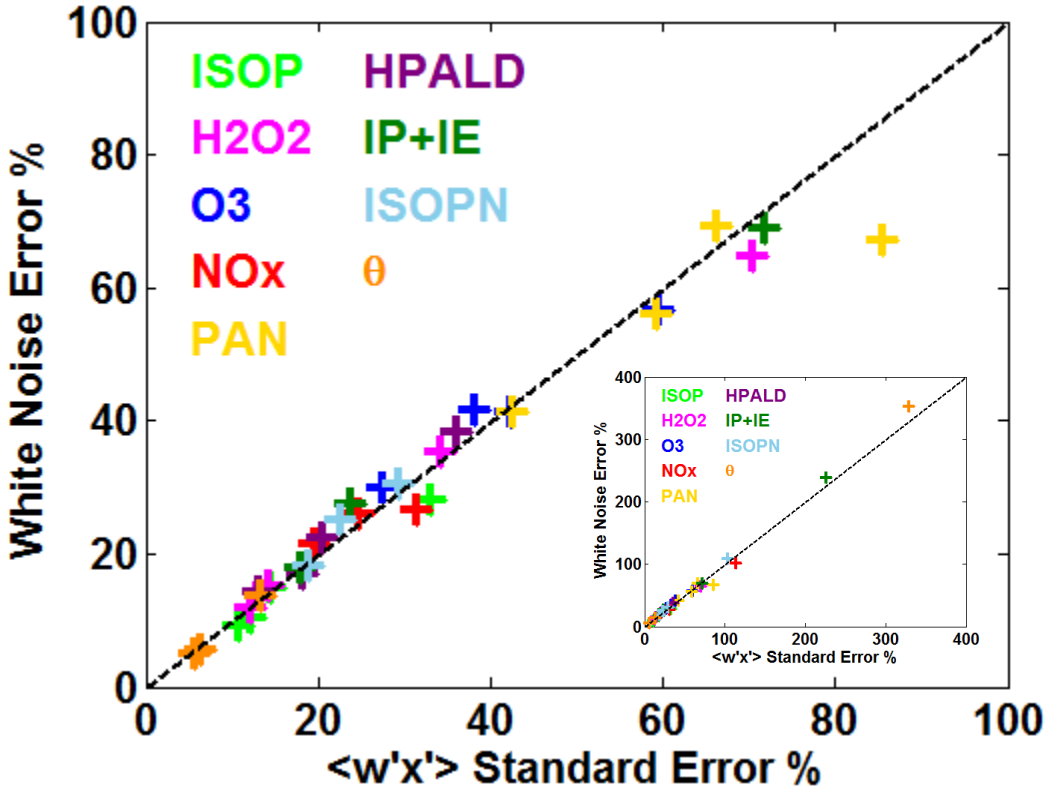

Figure S16. Comparison of 2σ errors in eddy covariance fluxes calculated via the covariance standard error and white noise covariance methods as described in the SI text. The dashed line has a slope of 1. The inset shows the same results with expanded axes.

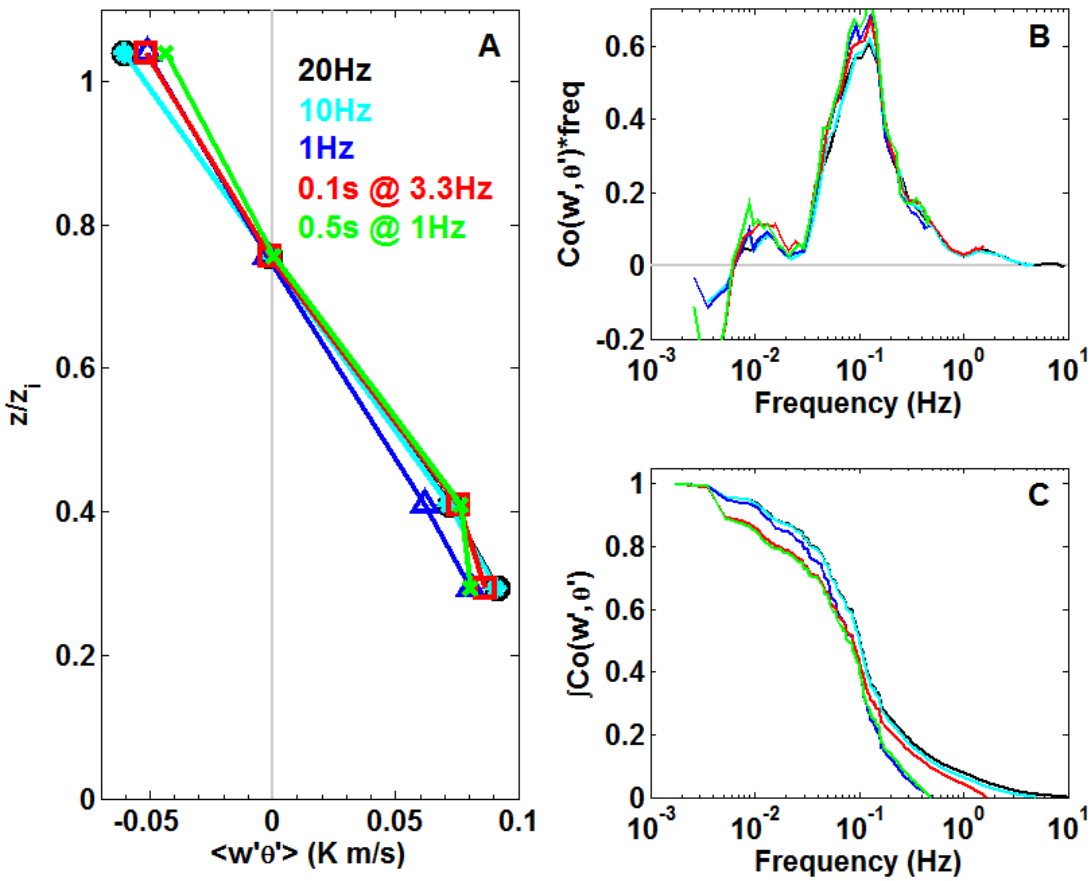

Figure S17. Potential temperature flux vertical profiles (A), cospectra (B) and ogives (C) for fluxes calculated using data averaged to different timescales. The vertical coordinate in (A) is normalized to the CBL height of 1060 m. Cospectra and ogives are from the lowest flight leg. Cospectra are normalized to their integrated area (total covariance). See also Table S3.

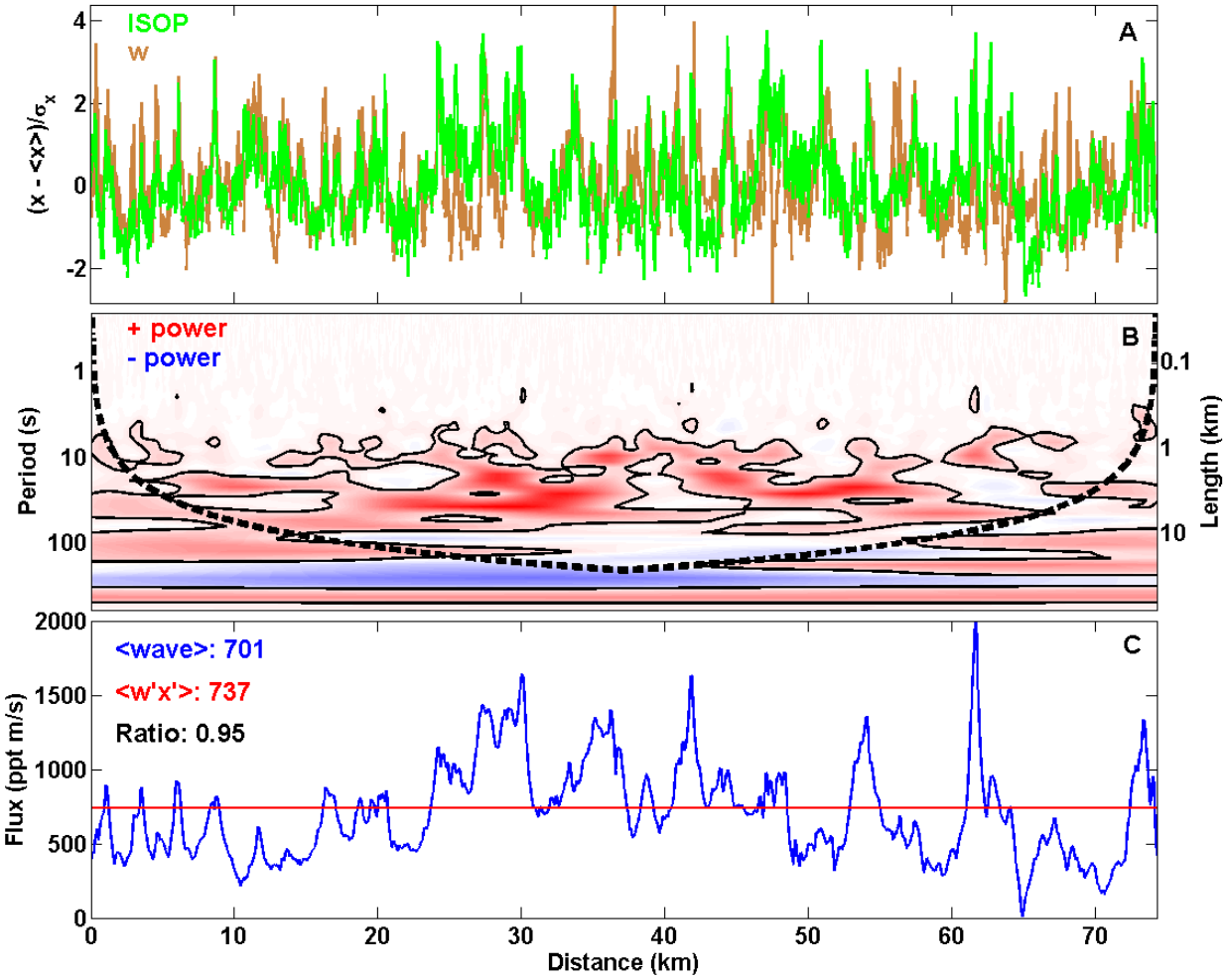

Figure S18. Example wavelet transform results for isoprene fluxes along the first flight segment. (A) Time series of instantaneous deviations from the segment mean (for w) or a 20-second running mean (for isoprene), normalized by standard deviation. (B) Local wavelet power co-spectrum of w' and ISOP'. Positive power contributions are shown in red, negative in blue. Contours enclose regions of >95% confidence relative to a red-noise process [*Torrence and Compo*, 1998]. The thick dashed line denotes the "cone of influence," below which edge effects may be important. (C) Integration over all frequencies gives the wavelet flux time series, which compares well with the average EC flux.

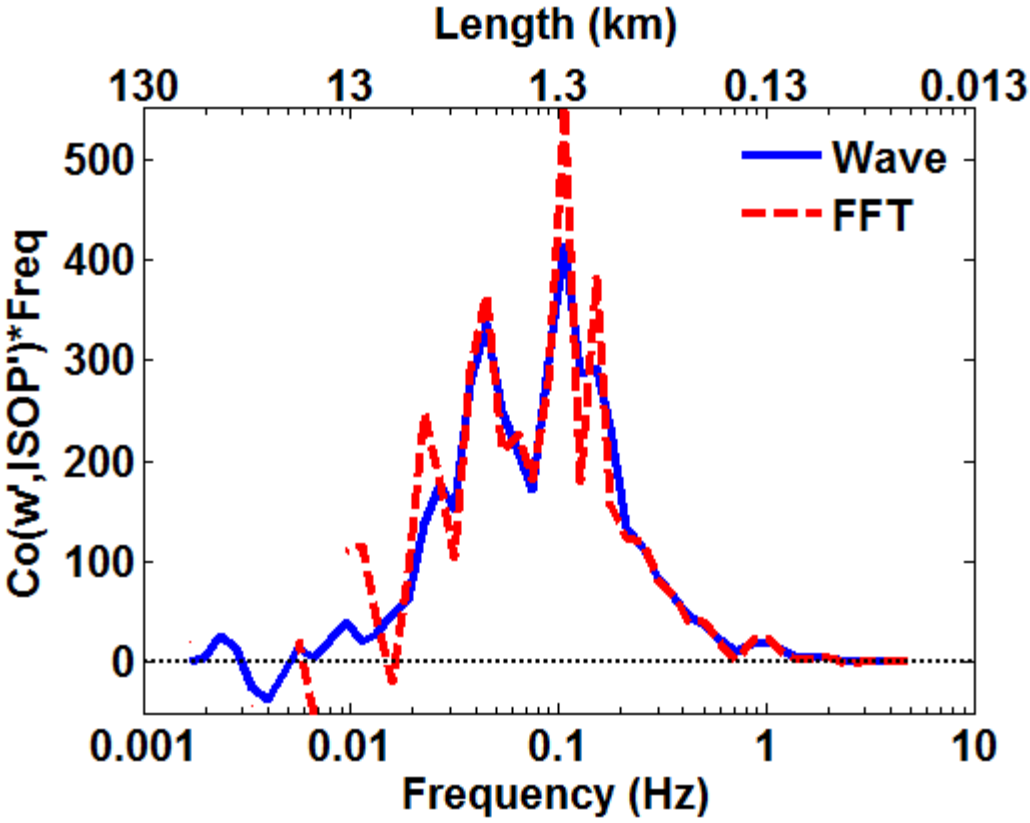

Figure S19. Comparison of wavelet and fourier transform frequency-multiplied cospectra for vertical wind and isoprene over the first flight segment.

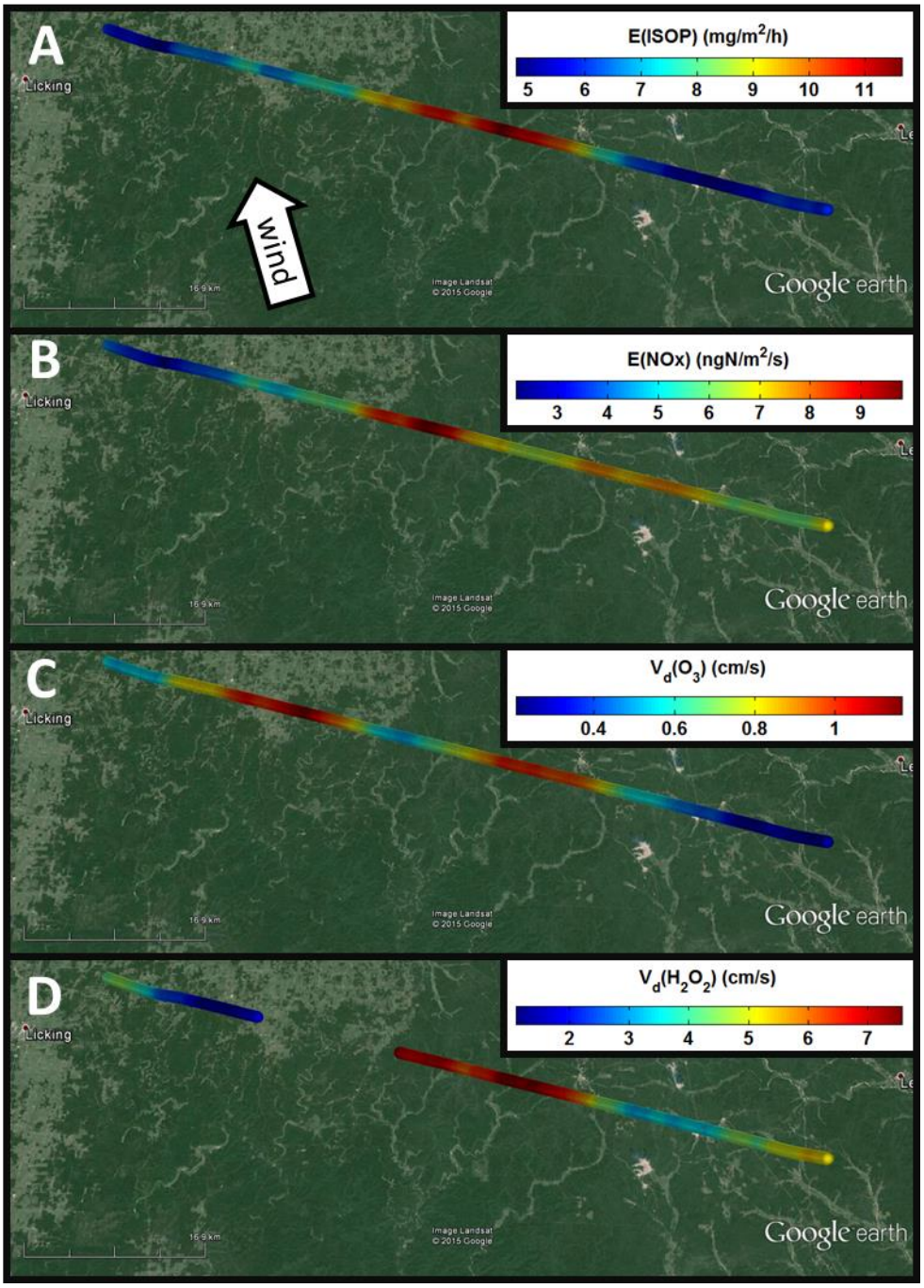

Figure S20. Map of wavelet-derived surface flux quantities: (A) Isoprene emission flux, (B) NO_x emission flux, (C) ozone deposition velocity, and (D) hydrogen peroxide deposition velocity. Quantities are based on wavelet fluxes for the first transect, corrected by a constant factor to account for divergence between the top of the canopy (assumed to be 20 m) and the measurement height. The underlying map is a satellite image of the study area.

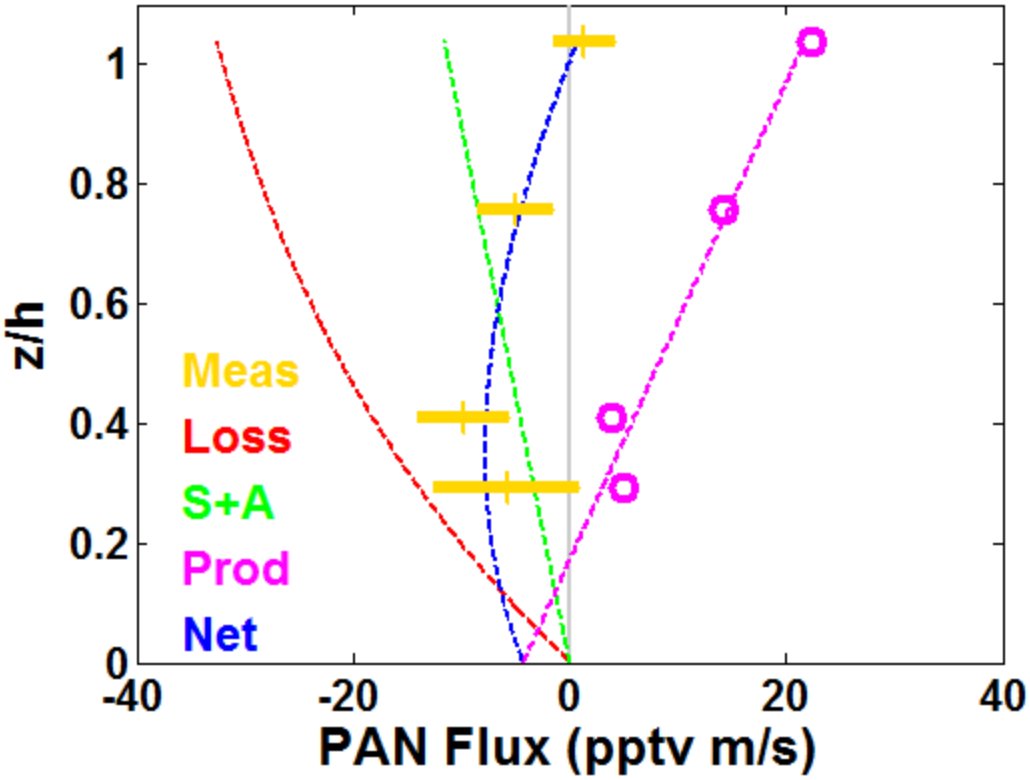

Figure S21. Observed and calculated components of the PAN flux vertical profile. Gold bars represent the mean and 95% confidence intervals for observed PAN fluxes. The green dashed line is the integrated storage and advection flux contribution. The chemical contributions consist of thermal decomposition losses (red line) and primary production of PA radicals (magenta circles and lines). The latter is determined as the residual of the sum of the measured, storage/advection fluxes minus the loss flux. The flux profile reconstructed from loss, production and storage/advection fluxes (blue line) agrees well with the observed profile.

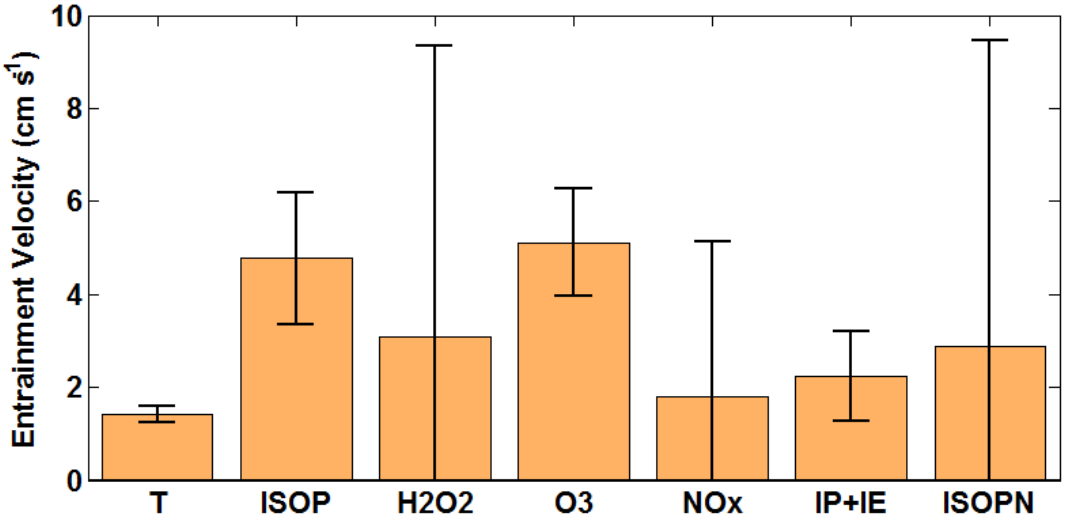

Figure S22. Entrainment velocities derived from observed fluxes and concentrations. Error bars represent 2σ uncertainties from propagated errors in least-squares fits to observed vertical flux profiles.

Table S1. Instrumentation used for flux calculations.

Measurement	Method	Sample Frequency	Calibration Accuracy	Ref.
3-D winds **T, potential T**	Radome Pt wire thermocouple	20 Hz	<1%	[*Chan et al.*, 1998]
Isoprene	Proton transfer reaction mass spectrometry	0.1s @ 3.3 Hz[a]		[*de Gouw and Warneke*, 2007]
NO **NO_2** **O_3**	Chemiluminescence	1 Hz	6% 8% 14%	[*Pollack et al.*, 2010; *Ryerson et al.*, 2000; *Ryerson et al.*, 1999]
PAN	Thermal dissociation + I^- chemical ionization mass spectrometry	0.5s @ 1 Hz[a]	15%	[*Slusher et al.*, 2004]
H_2O_2 **HPALD** **ISOPOOH + IEPOX** **ISOPN**	CF_3O^- chemical ionization mass spectrometry	10 Hz	60% 65% 60% 60%	[*Crounse et al.*, 2006; *Paulot et al.*, 2009a]

[a]Disjunct sampling.

Table S2. Summary of key results. Mean CBL mixing ratios are averaged over the first three segments (gray boxes in Fig. S2). Flux quantities, including the ground intercept (F_0) and flux divergence ($\partial F/\partial z$), are derived from uncertainty-weighted linear least-squares fits to vertical flux profiles unless otherwise specified. Storage ($\partial C/\partial t$) and along-track advection ($\overline{U_x}\ \partial C/\partial x$) are calculated as described in Sect. S3. Reported standard deviations (for concentrations) and uncertainties (for all other parameters) are 2σ.

Species	$\langle x \rangle_{CBL}$ pptv	F_0 pptv m s^{-1}	$\partial F/\partial z$ pptv s^{-1}	$\partial C/\partial t$ pptv s^{-1}	$\overline{U_x}\ \partial C/\partial x$ pptv s^{-1}	Q pptv s^{-1}
θ[a]	302.1	155	-0. 195	0. 175	-0.0017	-0.022
	± 0.5	± 4.9	± 0.006	± 0.032	± 0.0005	± 0.032
Isoprene	4700	858	-0.595	0.044	-0.025	-0.576
	± 2400	± 125	± 0.149	± 0.027	± 0.004	± 0.151
H_2O_2	1390	-66	0.065	0.006	0.0015	0.073
	± 180	± 5	± 0.005	± 0.014	± 0.0003	± 0.015
O_3	53000	-419	0.173	-0.244	0.132	0.061
	± 6000	± 58	± 0.081	± 0.247	± 0.007	± 0.260
NO	48	2.7	-0.002	-0.0001	0.0001	-0.002
	± 16	± 1.9	± 0.002	± 0.0005	± 0.0001	± 0.002
NO_2	126	12	-0.010	-0.013	0.0004	-0.022
	± 64	± 3	± 0.003	± 0.002	± 0.0001	± 0.004
NO_x	174	14	-0.011	-0.013	0.0005	-0.024
	± 71	± 5	± 0.006	± 0.003	± 0.0001	± 0.006
PAN[b]	232	---	---	-0.012	0.0015	---
	± 89			± 0.025	± 0.0001	
HPALD[b]	161	---	---	0.008	-0.0005	---
	± 39			± 0.009	± 0.0001	
ISOPOOH	1750	-32	0.071	0.164	-0.0067	0.228
+ IEPOX	± 486	± 9	± 0.016	± 0.023	± 0.0006	± 0.028
ISOPN[c]	119	-1.6	0.0052	0.003	-0.0005	0.008
	± 36	± 0.1	± 0.0001	± 0.002	± 0.0001	± 0.002

[a]Potential temperature. Units are K, mK m s^{-1}, and mK s^{-1}.
[b]Flux intercept and slope not reported because flux profiles are non-linear.
[c]Flux quantities based on linear fit excluding lowest altitude point.

Table S3. Fit results for kinematic heat flux profiles calculated with data averaged to various time bases.

Sample Frequency	$\partial F/\partial z$ mK m s^{-1}	F_0 K m s^{-1}	$\frac{\partial F/\partial z}{\partial F/\partial z(20\ Hz)}$	$\frac{F_0}{F_0\ (20\ Hz)}$	$\frac{F}{F\ (20\ Hz)}$ [c]
20 Hz	-0.195	0.155	1	1	1
10 Hz	-0.194	0.155	1.00	0.99	0.99
1 Hz	-0.171	0.135	0.88	0.87	0.86
0.1 s @ 3.3 Hz (disjunct)[a]	-0.187	0.150	0.96	0.97	0.95
0.5 s @ 1 Hz (disjunct)[b]	-0.173	0.142	0.88	0.91	0.89

[a]Mimics isoprene signal.
[b]Mimics PAN signal.
[c]Average of flux ratios for legs 1, 2 and 4. Leg 3 is excluded because fluxes are near 0.

Table S4. Reaction rate constants used in explicit chemical calculations described in Sect.S 4.

Reaction	Rate Expression or Photolysis Frequency	Source
ISOP + OH → $ISOPO_2$	$2.7\times10^{-11}\ \exp^{390/T}$	[*Atkinson et al.*, 2006]
ISOP + O_3 → products	$1.03\times10^{-14}\ \exp^{-1995/T}$	[*Atkinson et al.*, 2006]
$ISOPO_2$ + NO → 0.117 ISOPN + products	$2.7\times10^{-12}\ \exp^{360/T}$	[*Paulot et al.*, 2009a; *Saunders et al.*, 2003]
$ISOPO_2$ + HO_2 → 0.937 ISOPOOH + products	$2.06\times10^{-13}\ \exp^{1300/T}$	[*Liu et al.*, 2013; *Saunders et al.*, 2003]
$ISOPO_2$ + RO_2 → products	1.6×10^{-12}	[*Saunders et al.*, 2003][a]
$ISOPO_2$ → HPALD	$2\times10^{21}\ \exp^{9000/T} \times 2.06\times10^{-13}\ \exp^{1300/T}$	[*Crounse et al.*, 2011]
HPALD + OH → products	5.1×10^{-11}	[*Wolfe et al.*, 2012]
HPALD + O_3 → products	1.2×10^{-18}	[*Wolfe et al.*, 2012]
HPALD + h• → products	1.17×10^{-4}	Measured[c]
ISOPOOH + OH → products[b]	$3.8\times10^{-12}\ \exp^{200/T}$	[*Paulot et al.*, 2009b]
ISOPOOH + h• → products	4.5×10^{-6}	Measured[d]
IEPOX + OH → products	1.13×10^{-11}	[*Bates et al.*, 2014][a]
ISOPN + OH → products	3.47×10^{-11}	[*L Lee et al.*, 2014][a]
ISOPN + O_3 → products	1.99×10^{-18}	[*L Lee et al.*, 2014][a]
ISOPN + h• → products	1.37×10^{-6}	Measured[e]
HO_2 + HO_2 → H_2O_2	$(1 + 1.40\times10^{-21}\ \exp^{2200/T} \times [H_2O]) \times (2.2\times10^{-13}\ \exp^{600/T} + 1.9\times10^{-33}\ \exp^{980/T} \times [M])$	[*Atkinson et al.*, 2004]
H_2O_2 + OH → HO_2 + H_2O	$2.9\times10^{-12}\ \exp^{-160/T}$	[*Atkinson et al.*, 2004]
H_2O_2 + h• → 2OH	6.1×10^{-6}	Measured
OH + NO_2 → HNO_3	See note (f)	[*Atkinson et al.*, 2004]
PA + NO_2 ⇌ PAN	See note (f)	[*Atkinson et al.*, 2006]
PA + NO → products	$7.5\times10^{-12}\ \exp^{290/T}$	[*Atkinson et al.*, 2006]
PA + HO_2 → products	$5.2\times10^{-13}\ \exp^{980/T}$	[*Atkinson et al.*, 2006]
PA + RO_2 → products	$2 \times (3.5\times10^{-13} \times 2.9\times10^{-12}\ \exp^{500/T})^{0.5}$	[*Saunders et al.*, 2003]

[a]Isomer-weighted mean using modeled concentrations from 0-D UWCM base simulation. [b]Excluding IEPOX formation. [c]Using methacrolein photolysis frequency and assuming a quantum yield of 1 [*Wolfe et al.*, 2012]. [d]Using CH_3OOH photolysis frequency. [e]Using $CH_3CH_2ONO_2$ photolysis frequency. [f]Three-body reaction with complex rate coefficient. See IUPAC documentation.

Table S5. Calculated production and loss rates and chemical, deposition and heterogeneous loss lifetimes (τ) of isoprene oxidation products. Rates are averaged over the boundary layer.

Species	yield (α)	Production pptv s^{-1}	Loss pptv s^{-1}	Net pptv s^{-1}	v_d [a] cm s^{-1}	τ_{chem} (h)	τ_{dep} (h)[b]	τ_{het} (h)[c]
HPALD	0.08	0.048	0.030	0.017	2.4 ± 0.2	1.5	12	-
ISOPOOH + IEPOX	0.41	0.253	0.026	0.227	1.5 ± 0.4	18.5	19.9	66
ISOPN	0.05	0.032	0.006	0.026	1.1 ± 0.1	5.6	25.6	1.8

[a]Based on least-squares fits to flux profiles.
[b]Calculated as z_i/v_d.
[c]Lower limit calculated from missing flux, assuming this is entirely due to aerosol uptake.

Table S6. Comparison of HO_x concentrations calculated from flux divergence of isoprene (OH) and H_2O_2 (HO_2) with modeled concentrations from the GEOS-Chem global chemical transport model and the 0-D University of Washington Chemical Model (UWCM). Total RO_2 concentrations from the box model are also shown. Units for OH are 10^6 molecules cm^{-3}, and units for HO_2 and RO_2 are 10^8 molecules cm^{-3}. Uncertainties for flux-derived concentrations represent 2σ errors propagated from fits to flux profiles. Model-derived concentrations and uncertainties represent means and 2σ variability averaged over the first three flight legs. UWCM simulations include the base case with default MCM v3.2 chemistry and slow $ISOPO_2$ isomerization and four sensitivity simulations: faster $ISOPO_2$ isomerization (M1), reaction rate constant for OH + isoprene reduced by 50% to mimic reactant segregation (M2), and the physical loss rate constant reduced (M3a) or increased (M3b) by a factor of 2.

Species	Flux	GEOS-Chem	UWCM (base)	UWCM (M1)	UWCM (M2)	UWCM (M3a)	UWCM (M3b)
OH	1.3 ± 0.3	0.45 ± 0.07	1.0 ± 0.4	1.0 ± 0.4	1.5 ± 0.6	1.0 ± 0.4	1.0 ± 0.4
HO_2	5.8 ± 1.0	5.8 ± 0.4	6.6 ± 0.6	6.9 ± 0.6	6.9 ± 0.6	7.0 ± 0.7	6.3 ± 0.6
RO_2	---	---	10.4 ± 0.9	10.6 ± 1.0	10.0 ± 0.9	10.8 ± 1.0	10.1 ± 0.9